Pharmacological Research 211 (2025) 107560

Contents lists available at ScienceDirect

Pharmacological Research

journal homepage: www.elsevier.com/locate/yphrs

A hepatocellular carcinoma model with and without parenchymal liver damage that integrates technical and pathophysiological advantages for therapy testing

Karina Benderski [a,1], Paul Schneider [b,1], Panayiotis Kordeves [a], Michael Fichter [b,c], Jenny Schunke [b,e], Federica De Lorenzi [a,d], Feyza Durak [e], Barbara Schrörs [e], Özlem Akilli [e], Fabian Kiessling [f], Matthias Bros [b], Mustafa Diken [e], Stephan Grabbe [b], Jörn M. Schattenberg [g], Twan Lammers [a,d,*], Alexandros Marios Sofias [a,d,*], Leonard Kaps [b,g,**]

[a] Department of Nanomedicine and Theranostics, Institute for Experimental Molecular Imaging (ExMI), RWTH Aachen University Hospital, Forckenbeckstrasse 55, Aachen 52074, Germany
[b] Department of Dermatology, University Medical Center of the Johannes Gutenberg-University, Langenbeckstrasse 1, Mainz 55131, Germany
[c] Max Planck Institute for Polymer Research, Ackermannweg 10, Mainz 55128, Germany
[d] Mildred Scheel School of Oncology (MSSO), Center for Integrated Oncology Aachen (CIOA), RWTH Aachen University Hospital, Pauwelsstrasse 30, Aachen 52074, Germany
[e] TRON – Translational Oncology at the University Medical Center of the Johannes Gutenberg-University Mainz GmbH, Freiligrathstrasse 12, Mainz 55131, Germany
[f] Institute for Experimental Molecular Imaging (ExMI), RWTH Aachen University Hospital, Forckenbeckstrasse 55, Aachen 52074, Germany
[g] Department of Medicine II, Saarland University Medical Center, Saarland University, Kirrberger Strasse 100, Saarbrücken 66123, Germany

ARTICLE INFO

Keywords:
Hepatocellular carcinoma (HCC)
Liver cancer
Cirrhosis
Fibrosis
Nonalcoholic fatty liver disease
Nonalcoholic steatohepatitis
Immunotherapy
Cancer mouse model

ABSTRACT

Hepatocellular Carcinoma (HCC) is the most common form of primary liver cancer, with cirrhosis being its strongest risk factor. Interestingly, an increasing number of HCC cases is also observed without cirrhosis. We developed an HCC model via intrasplenic injection of highly tumorigenic HCC cells, which, due to cellular tropism, invade the liver and allow for a controllable disease progression. Specifically, C57BL/6JRj mice were intrasplenically inoculated with Dt81Hepa1–6 HCC cells, with a subgroup pre-treated with CCl_4 to induce cirrhosis (C-HCC). At four weeks post-inoculation, mice were sacrificed, and diseased livers were analyzed via histology, flow cytometry, and RT-qPCR to profile the extracellular matrix (ECM), angiogenesis, and immune cells. In addition, tumor-bearing mice were treated with the first-line therapy, AtezoBev, to assess therapeutic

---

Abbreviations: AFP, alpha-fetoprotein; Ang2, angiopoietin 2; AtezoBev, atezolizumab + bevacizumab; C, cirrhosis; CAF, cancer-associated fibroblast; β-Cat, β-catenin; CCl_4, carbon tetrachloride; Col, collagen; CTLA-4, cytotoxic T-lymphocyte-associated protein 4; DAPI, 4'-6-Diamidin-2-phenylindol; DAB, diaminobenzidine; DC, dendritic cells; DEN, diethylnitrosamine; ECM, extracellular matrix; FAP, fibroblast activation protein; FCS, fetal calf serum; FFPE, formalin-fixed paraffin-embedded; FGF, fibroblast growth factor; FN, fibronectin; GAPDH, glycerinaldehyd-3-phosphat-dehydrogenase; HCC, hepatocellular carcinoma; H&E, haematoxylin and eosin; HGF, hepatocyte growth factor; HIF1α, hypoxia-inducible factor 1-alpha; HSC, hepatic stellate cell; HYP, hydroxyproline; IGFR, insulin-like growth factor; IL, interleukin; ITGAE, integrin alpha E CD103; KC, Kupffer cell; KRB, krebs-ringer-buffer; LC, liver counterpart; L-selec, L-selectin; LYVE-1, lymphatic vessel endothelial hyaluronan receptor-1; M, macrophage; MFAP-5, microfibrillar-associated protein 5; MASH, metabolic dysfunction-associated steatohepatitis; MDM, monocyte-derived macrophage; MDSC, myeloid-derived suppressor cell; N, neutrophil; NK, natural killer cell; OS, overall survival; P4HA1, prolyl-4-hydroxylase subunit alpha-1; PD-1, programmed cell death protein 1; PD-L1, programmed cell death protein 1 ligand; PDX, patient-derived xenograft; PDGF, platelet-derived growth factor; PDGFRβ, platelet derived growth factor receptor beta; RFS, recurrence-free survival; RNAi, RNA interference; RNAseq, RNA sequencing; RT-qPCR, reverse transcription quantitative polymerase chain reaction; SHG, second harmonic generation; αSMA, smooth muscle actin; SFRS-4, serin/arginine-rich splicing factor 4; Stab, stabilin; TC, T cell; TGFβ, transforming growth factor beta; TME, tumor microenvironment; TNFα, tumor necrosis factor alpha; TPLSM, two-photon laser scanning microscopy; VEGF, vascular endothelial growth factor; VEGFR2, vascular endothelial growth factor receptor 2.

* Corresponding authors at: Department of Nanomedicine and Theranostics, Institute for Experimental Molecular Imaging (ExMI), RWTH Aachen University Hospital, Forckenbeckstrasse 55, Aachen 52074, Germany.

** Corresponding author at: Department of Dermatology, University Medical Center of the Johannes Gutenberg-University, Langenbeckstrasse 1, Mainz 55131, Germany.

E-mail addresses: tlammers@ukaachen.de (T. Lammers), asofias@ukaachen.de (A.M. Sofias), leonard.kaps@uks.eu (L. Kaps).

[1] Equal contribution (first authors): Karina Benderski, Paul Schneider.

https://doi.org/10.1016/j.phrs.2024.107560
Received 1 October 2024; Received in revised form 20 December 2024; Accepted 23 December 2024

responsiveness of the model. Dt81Hepa1–6 cells displayed similar gene expression as human HCC. After intrasplenic injection, all mice developed multifocal disease. C-HCC mice had a significantly higher tumor load than non-cirrhotic HCC mice. Both HCC and C-HCC models displayed extensive ECM formation, increased levels of vascularization, and immune cell infiltration compared to healthy and non-cancerous cirrhotic livers. AtezoBev treatment produced robust antitumor efficacy, validating the model's suitability for therapy testing. In conclusion, we established a rapidly developing and high-yield HCC model through a simple intrasplenic injection, with or without cirrhotic damage. The model overexpressed key human HCC genes and showed high responsiveness to first-line treatment. Our model uniquely combines all the above-mentioned features, promoting its use towards HCC therapy testing.

1. Introduction

Hepatocellular carcinoma (HCC) is the most frequent primary liver cancer, and the third leading cause of cancer-related deaths [1–3]. The development of HCC is a multi-step process, which is led by genetic and epigenetic changes in hepatocytes, giving rise to cancer stemness [4,5]. Over 90 % of HCC cases arise from cirrhotic livers. Cirrhosis is the end-stage of chronic liver disease, characterized by excessive accumulation of extracellular matrix (ECM), scarring, and compromised organ function [6,7]. However, HCC is also increasingly diagnosed in patients with metabolic dysfunction-associated steatohepatitis (MASH) without underlying cirrhosis [8,9].

Liver fibrosis and tumor presence are typically asymptomatic in the early stages. Therefore, many patients are diagnosed with HCC only with advanced disease. At this stage curative options like transplantation or resection are futile, and patients can only be considered for systemic therapy with the checkpoint inhibitor atezolizumab (anti-PD-L1) in combination with the anti-angiogenic antibody bevacizumab (anti-VEGF) or different ablation methods (e.g. radiofrequency ablation, transcatheter arterial chemoembolization) [10–12]. The tumor microenvironment (TME) plays a key role in HCC development and treatment response and it has recently emerged as an important target for anticancer therapies [13,14]. TME refers to the complex ecosystem surrounding cancer cells that includes immune cells, stromal cells, blood vessels, and ECM. In HCC, key TME features such as immunosuppressive cells, cancer-associated fibroblasts (CAF) and abnormal vasculature create an immunosuppressive microenvironment, promote angiogenesis, and enable immune escape, thereby supporting tumor growth [15]. The variable response to current treatments highlights the inherent diversity and heterogeneity of HCC among individual patients. Consequently, there is an ongoing need for extensive research on HCC therapies, emphasizing the demand for robust, reliable, and applicable preclinical models.

Developing adequate preclinical murine models for HCC is challenging due to the complexity of chronic liver diseases, ethical approval, and technical implementation. The ideal model should reflect the HCC environment across different stages of the disease progression, including the manifestation of certain cell death pathways, injury extent, scar tissue presence, and immune cell composition. Currently, the *in vivo* models for studying HCC in immunocompetent hosts are limited and mainly comprise genetically engineered, diet-, and chemical-induced models [16]. Among those, the formation of cirrhosis and HCC via administration of carbon tetrachloride (CCl_4), a highly fibrogenic hepatotoxin, is well established [17]. Combining CCl_4 with diethylnitrosamine (DEN), as a second hepatotoxin, increases the probability of HCC development. However, this model is time-inefficient (20 weeks for tumor development), highly heterogeneous in terms of tumor size, and has a low yield (only 50 % of the animals develop tumors). Furthermore, DEN is highly mutagenic and the induced mutanome does not overlay with the genetic alterations found in patients [18]. In other commonly used models the combined administration of DEN and the tumor promoter phenobarbital leads to a slow and heterogenous tumor development after several months [19].

To avoid the use of toxic substances, syngeneic models based on the direct injection of HCC cells into the liver of immunocompetent animals have been developed as an alternative. Such models can be combined with inflammation and fibrosis induction by CCl_4 gavage, to mirror HCC development in chronic liver diseases [20]. However, an intrahepatic injection is both, technically challenging and often induces only a monofocal disease, and therefore does not accurately mimic the clinical appearance of HCC [21,22]. Additionally, murine cell lines that are used for this purpose, e.g., Hepa1–6 are characterized by low tumorgenicity *in vivo*.

We here set out to develop a syngeneic HCC animal model that manifests as multifocal disease, which resembles the clinical scenario. To achieve this, we used a novel cell line, namely Dt81Hepa1–6, derived from *in vivo* passaging of Hepa1–6 cells in C57BL/6 mice. During the passaging process, cells were selected according to high tumorigenicity, rapid tumor development and high liver tropism [23]. In combination with intrasplenic injection an exclusive multifocal liver disease with high yield is easily achievable. Additionally, to develop a cirrhotic HCC model, we combined the HCC intrasplenic injection with prior CCl_4 administration. Four comparative groups (healthy liver control, cirrhotic liver control, HCC, cirrhotic HCC) were created and the dissected livers and tumor lesions were extensively analyzed for their protein and immunological profile. To evaluate the model's responsiveness to clinically relevant therapies, diseased mice were challenged with the combination therapy of anti-PD-L1 and anti-VEGF antibodies, resembling the first-line treatment of atezolizumab and bevacizumab, i.e., AtezoBev. Overall, we present a mouse model, which is intended to address current gaps in preclinical models. We combined advantageous features of existing models which lack in aspect, e.g., the use of immunocompetent wildtype mice, switchable cirrhotic or non-cirrhotic phenotype, multifocal disease but allowing a straightforward cell inoculation, short experimental cycles and high tumor development yields. Finally, our model shares major HCC key genes observed in the clinical situation and is, due to the responsiveness to clinical therapy, relevant for translational approaches.

2. Materials and methods

2.1. Cell lines

Dt81Hepa1–6 HCC cells (C57BL/6, male, passage no.5, provided by M. Bilodeau, CHUM, Montreal, Canada) [23], MHSC-SV40 hepatic stellate cells (C57BL/6, passage no.3, ABM Inc., Richmond, Canada), NIH/3T3 fibroblasts (NIH/Swiss, male, passage no.2, ATCC, Manassas, VA, USA), SVEC4–10 endothelial cells (C3H/HeJ, male, passage no.9, ATCC, Manassas, VA, USA), RAW264.7 macrophages (BALB/c, male, passage no.5, ATCC, Manassas, VA, USA) and B16/F10 melanoma cells (C57BL/6 J, male, passage no.8, ATCC, Manassas, VA, USA) were cultured in Dulbecco's Modified Eagle's Medium (DMEM; Invitrogen, Darmstadt, Germany). Additionally, DC2.4 dendritic cells (C57BL/6, passage no.6, Sigma Aldrich, Taufkirchen, Germany) were cultured in RPMI-1640 medium (Sigma Aldrich, Taufkirchen, Germany) and AML-12 hepatocytes (CD-1, male, passage no.6, ATCC, Manassas, VA, USA) were cultured in DMEM:F12 medium (Sigma Aldrich, Taufkirchen, Germany). Media were supplemented with 10 % fetal calf serum (FCS;

Invitrogen, Darmstadt, Germany) and 1 % Penicillin/Streptomycin (Pen/Strep; Invitrogen, Darmstadt, Germany) as well as 1 % L-glutamine (Invitrogen, Darmstadt, Germany). Medium for AML-12 cells additionally contained 10 μg/mL insulin, 5.5 μg/mL transferrin, 5 ng/mL selenium (ITS-G; Gibco, Darmstadt, Germany) and 40 μg/mL dexamethasone (Sigma Aldrich, Taufkirchen, Germany). All cells were incubated in T75 cell culture flasks (Cell Star, Greiner, Kremsmünster, Austria) at 37 °C in 5 % CO_2. Media was changed every two days and the cells detached by trypsinization (0.05 % Trypsin-EDTA in PBS) prior to reaching confluency.

2.2. Total RNA extraction, library preparation and directional mRNA Sequencing

Total RNA was extracted from frozen dry cell pellets using Qiagens RNeasy Mini Kit. Quantity and quality were assessed using the Qubit 3 fluorometer with the RNA BR AssayKit (Invitrogen; Darmstadt, Germany) and the Agilent Bioanalyzer 2100 system using the RNA Pico kit.

RNA exome capture libraries were prepared in duplicates with an input of 100 ng total RNA each. The RNA sample was fragmented, primed, reverse-transcripted, end-repaired and adenylated followed by ligation of sequencing adaptor and the appropriate eight-nucleotide NEXTFLEX DNA barcode (Perkin Elmer; Waltham, Massachusetts, USA). Pre-amplification of the library was done using the KAPA Hyper Prep kit (Roche; Darmstadt, Germany). Subsequently, target regions were hybridized to biotinylated baits (SureSelectXT Human All Exon v6 and SureSelect XT Reagent kit, Agilent) and isolated using streptavidin-coated magnetic beads (Invitrogen). The post-capture library was then amplified with the KAPA Library Amplification kit (Roche; Darmstadt, Germany). All intermediate and final library purification steps were carried out using AMPure XP beads (Beckman Coulter; Brea, California, USA). Final library quantity and quality was assessed using the Qubit 3 fluorometer with Qubit dsDNA HS Assay Kit (Invitrogen; Darmstadt, Germany) and the BioAnalyzer with High Sensitivity DNA Kit (Agilent; Santa Clara, California, USA).

All libraries were sequenced in paired-end mode (2 ×50 nt) on an Illumina NovaSeq 6000 instrument resulting in around 80 million distinct sequencing reads per library.

2.3. Differential expression analysis

RNA-seq raw reads of the Dt81Hepa1–6 cell line (technical duplicates) and four publicly available murine primary hepatocyte samples (SRR12400465, SRR12400465, SRR12400467, SRR12400467; downloaded from https://www.ebi.ac.uk/ena/browser/view/PRJNA655673) were subjected to quality control with FastQC (v0.11.9, www.bioinformatics.braham.ac.uk/projects/fastqc/) and FastQ Screen (v0.15.1) [24] and subsequently processed with kallisto (v0.42.4) [25] and the *Mus musculus* reference GRCm38 (ENSEMBL release 84). Estimated read counts were summarized per gene and used for differential expression analysis with DESeq2 (version 1.24.0) [26]. Log2-fold change values after “apeglm” shrinkage and BH (Benjamini-Hochberg) adjusted p-values are visualized as Volcano plot [27]. Genes with BH adjusted p-values < 0.05 and $|\text{log2-fold change}| > 1$ were considered as significantly regulated [28]. Pearson’s correlation or sample-to-sample distances were determined based on all genes with annotated orthologs or genes of the SMITH_LIVER_CANCER MSigDB gene set (PMID: 12591738, https://www.gsea-msigdb.org/gsea/msigdb/cards/SMITH_LIVER_CANCER). ($n = 2$ for Dt81Hepa1–6, $n = 4$ for primary hepatocytes).

2.4. Animals

Animal studies were approved by local authorities (Landesunteruchungsamt (LUA) Rhineland-Palatinate, Germany) with the reference number G20–1–130. Experiments were carried out according to World Medical Association (WMA) and European Union (EU, directive 2010/63/EU) guidelines. Wildtype male C57BL/6 mice were purchased from Janvier (Le genest-Saint-Isle, France) and kept under 12 h light-dark cycles at 25 °C and 40–60 % humidity with daily human care. The animals had access to regular chow and water *ad libitum*. At predetermined timepoints, mice were sacrificed by cervical dislocation. To guarantee animal welfare and humane endpoints, mice were inspected daily and scored on experiment-specific pathophysiological characteristics twice per week. Sample size was determined based on *a priori* G*Power analysis via a two-tailed *t*-test, with α error probability = 0.05, and power (1-β error probability) = 0.9.

2.5. Intrasplenic injection of Dt81Hepa1-6 HCC cells

Dt81Hepa1–6 HCC cells were cultivated in DMEM at 37 °C in 5 % CO_2 and freshly harvested before inoculation. For that, cells were trypsinized, washed 3 x with PBS and resuspended in PBS. The cell aliquot ($5 \cdot 10^5$ cells per 150 μL) was aspirated in 21 G syringes for intrasplenic injection. 6-week-old mice were anesthetized with ketamine/xylazine and analgesized with metamizole (200 mg/kg s.c.) to perform a left-side laparotomy. The spleen was mobilized, and the well-mixed cell suspension was carefully injected into the spleen parenchyma. When the spleen reperfused with blood, the needle was withdrawn and the puncture sealed with a droplet of vetbound veterinary glue (Histoacryl®, B.Braun, Melsungen, Germany). The spleen was relocalized into the abdominal cavity, the peritoneum closed with biodegradable suture (Coated VICRYL™, Ethicon®, Raritan, NJ, USA), and the skin with wound clips. For post-surgical analgesia, the drinking water was supplemented with 1.5 mg/mL metamizole for 2 days.

For the second model (cirrhotic HCC; C-HCC), advanced liver fibrosis/ early cirrhosis was induced prior to cell inoculation. Briefly, mice were gavaged with carbon tetrachloride (CCl_4; Sigma Aldrich, Taufkirchen, Germany). During a period of six weeks, mice received three oral administrations per week with increasing concentrations (gavage week 1–2: 1 mL/kg, 3–4: 2 mL/kg, 5–6: 3 mL/kg) of CCl_4 diluted to administrable volumes (150 μL) in mineral oil (Ph. EUR., Carl Roth, Karlsruhe, Germany). Following a rest phase of 1 week, Dt81Hepa1–6 cells were inoculated as described above. Mice were sacrificed by cervical dislocation 14 or 28 days post Dt81Hepa1–6 inoculation. To provide a better age-balanced comparison between both models, in the non-cirrhotic HCC model, mice did not undergo any experimental intervention for the first 7 weeks before receiving intrasplenic injections of Dt81Hepa1–6 cells. This step is not required for later use of the HCC model.

For the control groups, mice were gavaged with CCl_4 for 6 weeks and sacrificed 5 weeks thereafter (cirrhotic liver control). For the healthy liver control, mice did not receive any experimental intervention for 11 weeks before sacrification. To study pathophysiological changes following CCl_4 administration, mice were either treated with CCl_4 for 6 weeks and subsequently remained untreated for 1 week or did not receive any treatment (for seven weeks) before sacrification.

2.6. Hydroxyproline determination

Total liver collagen content was determined with an hydroxyproline (HYP) assay as previously described [29]. Liver specimens, collected randomly from different liver lobes (10–20 mg), were snap-frozen and minced using a cryo-mortar. Samples were lysed in 1 mL of 6 M HCl at 110 °C for 16 h in an orbital shaker. Following that, 400 μL of 10 M NaOH was added and triplicates of 5 μL were placed in 96-well plates (Greiner, Kremsmünster, Austria). The samples were mixed with 95 μL at 0.1 M citrate buffer at pH 6, and 100 μL of oxidation solution (6 mg/mL chloramine-T in 0.1 M citrate buffer) and incubated for 15 min on an orbital shaker at RT. Subsequently, 100 μL of freshly prepared Ehrlich’s reagent (2.48 g dimethyl-benzaldehyde dissolved in 7.27 mL *i*PrOH and 2.73 mL $HClO_4$ (70 %)) was added. Following a reaction time of 30 min at 65 °C on an orbital shaker, the absorbance was measured at 570 nm with an Infinite M200Pro spectrophotometer (TECAN, Männedorf, Switzerland). Total HYP (µg/ mg liver weight) was normalized to individual liver weights. (n = 3–4)

2.7. AFP determination

To quantify AFP levels from murine sera or cell culture supernatant, a Quantikine® Colorimetric Sandwich ELISA Kit (R&D, Abingdon, UK) was used according to the manufacturer's protocol. The OD_{450} was determined using a TECAN Infinite M200Pro spectrophotometer. Reactions were performed in duplicates (n = 2). Further data analysis was performed using Graphpad Prism software (v. 9.5.1). The goodness of regression is expressed by R^2. (n = 65)

2.8. Immunohistochemistry staining of cryopreserved tissue

Liver tissue was embedded in optimal cutting temperature matrix compound (Tissue-Tek® O.C.T., Sakura Finetek, Umkirch, Germany) and cryopreserved at −80 °C. Tissue was sectioned at 8 µm thick slices and stained for different markers using fluorescently labeled antibodies. Slides were washed with PBS for 2 min to remove the embedding Tissue Tek material and fixed with 80 % methanol for 5 min and ice-cold acetone for 2 min. Following 3 washing steps with PBS, primary antibodies were applied in 12 % BSA, and samples were incubated overnight at 4 °C. After that, slides were washed with PBS and incubated with the respective secondary antibodies diluted in 12 % BSA for 45 min at room temperature together with 4′,6-Diamidin-2-phenylindol (DAPI; Thermofischer, Waltham, MA, USA). Finally, slides were washed with PBS, mounted with Mowiol® 4–88 (anti-fade agent; Carl-Roth, Karlsruhe, Germany), and glass-covered for further fluorescence microscopy analysis.

Antibodies and dilutions used were as follows: Primary: anti-Col-I (1:100; #r1038, OriGene, Rockville, USA), anti-FN (1:100; #ab2413, abcam,UK), anti-Col-IV (1:100; #20451, Novotec, Germany), anti-CD34 (1:100; #ab81289, abcam,UK), anti-αSMA (1:100; #BK610501, Progen, Germany), anti-VEGFR2 (1:20; #AF644, R&D Systems,USA), anti-PDGFRβ (1:200; #ab32570, abcam, UK). Secondary: Cy3 anti-Rabbit (1:500; #711–166–152), Alexa Fluor 488 anti-Rat (1:350; #-546–153), and Cy3 anti-Biotin (1:500; #016–160–084) from dianova, Eching, Germany.

2.9. Fluorescence microscopy

Fluorescence microscopy was performed using a Zeiss® Axio imager M2 fluorescence microscope (Carl-Zeiss Microscopy GmbH, Jena, Germany). Up to 16 images per mouse were taken from areas of the tumor and liver tissue counterpart at 20x magnification. For the analysis of tumor regions from 2-week and 4-week growth a magnification of 40x was used. Images were analyzed with open-source program Fiji/ImageJ. Results are displayed as area fraction percentage. Detailed results for each individual mouse are displayed in Fig. S1-S3. (biological replicates: n = 3–4; technical replicates: n = 9–16)

2.10. Immunohistochemistry staining of paraffin-embedded tissue

Harvested livers were fixed in 10 % neutral-buffered formalin for 48 h. Tissues were then embedded in paraffin following standard histological procedures. Formalin-fixed paraffin embedded (FFPE) blocks were cut into 5 µm thick slices with a microtome. Antigen retrieval was performed at 60 °C for 2 h followed by tissue deparaffinization using xylol and ethanol serial dilution for 1 h. For Haematoxylin and eosin (H&E), Masson's trichrome, and Sirius red staining standard protocols were followed [29,30].

For antibody staining, endogenous peroxidase activity was blocked by using 0.3 % hydrogen peroxide containing PBS for 10 min, and slides were incubated with primary antibodies diluted in 12 % BSA for 60 min. FFPE slides were subsequently washed with PBS and incubated with secondary antibodies for 45 min. Thereafter, FFPE slides were washed with PBS and staining was developed with diaminobenzidine (DAB; Carl Roth, Karlsruhe, Germany). After an additional PBS washing step cell nuclei were visualized with haematoxylin and the stainings were preserved using ethanol and xylol serial dilution. Stained FFPE sections were mounted with Vitro-Clud® (R. Langenbrinck GmbH, Emmendingen, Germany). HIF1α staining was performed on 3 µm FFPE tissue sections and stained in the Leica BOND Rx autostainer. The standard IHC protocol adjusted to 30 min primary antibody incubation with heat-induced epitope retrieval: 20 min ER2 was used. The staining was detected using BOND Polymer Refined Detection Kit (Leica, DS9800).

Antibodies and dilutions used were as follows: Primary: anti-CD31 (1:50; #dia310, dianova, Eching, Germany), anti-αSMA (1:200; #ab5694, abcam, UK), anti-PDGFRβ (1:500; #ab32570, abcam, UK), anti-VEGFR2 (1:400; #AF644, R&D Systems, USA), anti-CD68 (1:100; #ab125212, acam, UK), anti-CD4 (1:2000; #ab183685, abcam, UK), anti-CD8 (1:2000; #ab217344, abcam, UK), anti-Ly6G (1:1000; #ab238132, abcam, UK), anti-HIF1α (1:2000, #487085, Cell signaling, USA). Secondary: HRP Horse Anti-Rabbit IgG and HRP and Goat Anti-Rabbit IgG (#MP-7401; Vector Laboratories, Newark, USA).

2.11. Brightfield microscopy

Overview images of FFPE slides were acquired using the Fritz Microscope (PreciPoint, Garching b.M., Germany) at 20x. Up to 16 Images of respective tumor and liver counterpart areas per mouse were selected from the overview images, using QuPath 5.0. Images were processed with open-source program Fiji/ImageJ. Results are displayed as area fraction. Detailed results for each individual mouse are displayed in Fig. S4-S5. (biological replicates: n = 3–4; technical replicates: n = 9–16)

2.12. Two-photon laser scanning microscopy

Tissue slices were cryosectioned at 70 µm thickness for two-photon laser scanning microscopy (TPLSM; FV1000MPE Multiphoton Microscopy System, Olympus, Hamburg, Germany). SYTO™ Red Fluorescent Nucleic Acid Stain (ThermoFischer Scientific, Waltham, MA, USA) was diluted in water (1:100) and added on top of the slices and the tissue was visualized using a 25x water-immersed objective. Collagen fibers were monitored via second harmonic generation (SHG) imaging. 50 Z-stacks, with the dimension of 500 µm x 500 µm x 50 µm, were obtained. 4 Images per mouse were captured from tumor sections and liver tissue counterparts, respectively, and the fluorescence signal was obtained through the photo-multiplier tubes adjusted for the optimal emission spectra. Collagen volume was retrieved by using the Imaris Software version 9.4 (Bitplane AG, Schlieren, Switzerland). The collagen fiber thickness was calculated using the trabecular thickness feature of the BoneJ plugin in the image processing package of Fiji. (biological replicates: n = 3–4; technical replicates: n = 4)

2.13. Reverse transcription quantitative polymerase chain reaction

Total RNA was extracted from cultured cells or murine liver tissue using Monarch™ Total RNA Miniprep Kit (New England BioLabs, Frankfurt a.M., Germany) following the manufacturer's protocol. Extracted RNA was directly subjected to RT-qPCR using Luna® Universal One-Step RT-qPCR Kit (New England BioLabs, Frankfurt a.M., Germany). Reactions were performed according to the manufacturer's protocol. Amplification was performed using the C1000 thermal cycler (Bio-Rad, Hercules, CA, USA) under the following reaction conditions: 55 °C for 10 min, 95 °C for 1 min followed by 40 cycles of 95 °C for 10 s and 60 °C for 1 min. Results were calculated using the ΔΔCt method and SFRS-4 or GAPDH as reference gene. Details of the PCR primer sequences (ordered at Eurofins, Luxembourg) used in this work are displayed in supplementary table 1. mRNA expression was analyzed for Col-I, Col-IV, Col-VI, P4HA1, FN, Ang2, stab, LYVE-1, αSMA, PDGFRβ, FAP, TGF-β, HGF, FGF, TNFα, PDGF, IGFR, interleukins, L-selec and β-cat. (n = 6).

2.14. *Generation of liver single cell suspensions*

Freshly dissected livers were carefully rinsed with Krebs Ringer Buffer (KRB, pH 7.4). Following removal of the gall bladder, livers were digested with 5.000 U/mL of collagenase IV (Gibco, Carlsbad, CA, USA) and 10.000 U/mL DNAse I (ThermoFisher Scientific, Waltham, MA, USA) in KRB. The organs were carefully homogenized with a gentleMACS™ dissociator (Milteny, Bergisch Gladbach, Germany) and incubated for 30 minutes at 37 °C in an orbital shaker. The suspension was filtered through a 100 µm cell strainer and centrifuged at 300 x g for 10 min to collect parenchymal and non-parenchymal cells. To remove adjacent erythrocytes, the cell pellet was resuspended in 4 mL of Gey's lysis buffer (155 mM NH_4Cl, 10 mM $KHCO_3$, 100 µM EDTA; pH=7.4) and incubated for 1 min at RT. Following three washing steps with PBS, the cells were immediately subjected to further analysis.

2.15. *Flow cytometry*

Freshly prepared liver single cell suspensions were stained with fluorochrome-labeled antibodies according to the manufacturer's protocol. The following antibodies were used to discriminate specific cell populations: leukocytes (CD45^{+}), dendritic cells (DC: CD45$^{+}_{,}$ CD11c^{+}), Kupffer cells (KC: CD45^{+}, F4/80^{+}, CD11b^{-}), monocyte-derived macrophages (MDM; CD45^{+}, F4/80^{+}, CD11b^{+}), natural killer cells (NK: CD45^{+}, NK1.1^{+}), myeloid-derived suppressor cells (MDSC; CD45^{+}, Ly6C^{+}, Ly6G^{-}), neutrophils (N: CD45^{+}, Ly6G^{+}, F4/80^{+}), T cells (TC; CD45^{+}, CD3^{+}). Following additional antibodies were used for activation analysis in the pregated populations: For DC (CD80^{+} or CD86^{+} or CD103^{+}), for M1 macrophages (CD80^{+}CD86^{+}), for M2 macrophages (CD206^{+}), for MDM-M1 (Ly6C^{+}), for MDM-M2 (Ly6C^{-}), for NK cells (CD11b^{+}), for TC (CD4^{+} and CD28^{+} or PD-1^{+} or CTLA-4^{+} or PD-L1^{+}; and CD62L^{+} or CD44^{+} or CD25^{+} or CD69^{+}; CD8^{+} and CD28^{+} or PD-1^{+} or CTLA-4^{+} or PD-L1^{+}; and CD62L^{+} or CD44^{+} or CD25^{+} or CD69^{+}). Unspecific antibody binding was prevented by blocking CD16/CD32 (EPR23501–203, abcam, Cambridge, UK). Dead cells were excluded using the Fixable Viability Dye™ (FVD) eFluor™ 506 (eBioscience, Frankfurt a.M., Germany). Cells were fixed with 4 % PFA for 15 min at RT and immediately subjected to flow cytometry. $1–5{\cdot}10^5$ cells were measured per staining using an Attune NxT Flow Cytometer (ThermoFisher Scientific, Waltham, MA, USA). Compensation was performed with OneComp eBeads (eBioscience, Frankfurt a.M., Germany) and calculated by Attune NxT software. Data was further processed by FlowJo Software v.10.8.1 (BD Biosciences, Heidelberg, Germany). Gating strategies are illustrated in Fig. S6**-7**.

Antibodies used were: CD45-SB702 (#67–0451–82; Invitrogen; Waltham, MA, USA); CD11c-FITC, CD3-PE-Cy5 (#557400), CD8-PE (#553033), F4/80-FITC (#11–4801–85) and FITC-CD25 (#553072 (BD Biosciences, Heidelberg, Germany); Ly6G-PE-eFl610 (#61–9668), Ly6c-PerCp-Cy5.5 (#45–5932–82), CD4-AF700 (#56–0042–82), CD80-PerCp-eFl710 (#46–0801–82), CD86-eFl450 (#48–0862) and CD68-PE-Cy7 (#25–0681), APC-CD62L (#17–0621–81), PE-CD44 (+12–044182) (Thermo Fischer, Waltham, Massachusetts, USA); CD28-FITC (#HM3501; CALTAG, Waltham, Massachusetts, USA); NK1.1-PE (#108407), CD16/32 (#101320), CD11b-BV421 (#101235), CD206-AF647 (#141712), CD103-PE (#121405), PD-L1-BV605 (#124321), CTLA4-APC (#106309), and BV711-CD69 (#310944) BioLegend, San Diego, California, USA)). (n = 6 for healthy vs. cirrhotic liver; n = 5–8 for HCC vs. C-HCC)

2.16. *Bevacizumab/atezolizumab first line treatment*

Animals with or without prior induced cirrhosis were intrasplenically injected with Dt81Hepa1–6 cells as described above (Section 2.5). For intraperitoneal (i.p.) injections an anti-VEGF antibody (analogue to bevacizumab) was purchased from Roche (Basel, Switzerland) and an anti-PD-L1 antibody (hpdl1-mab9-b, analogue to atezolizumab) was purchased from Invitrogen (Waltham, MA, USA). I.p. injections were performed on day 7, 14 and 21 post HCC injection with concentrations of 8 mg/kg per antibody, while controls received equal volumes of saline (0.9 % NaCl), according to literature [31]. Healthy mice that did not receive tumor cell injection or any above indicated treatment were used as a second control group. On day 28 post cell injections animals were sacrificed to analyze the organs. (n = 5).

2.17. *Statistical analysis*

Data are presented as means ± SD. Statistical differences among groups were identified via an unpaired two-tailed Student's *t*-test, one-way ANOVA, or RM two-way ANOVA with Tukey's correction. *P* values < 0.05 indicate significant differences. All statistical analyses were performed using GraphPhad Prism 10.2.2 (San Diego, CA, USA).

3. Results

3.1. *HCC development in the presence and absence of advanced liver fibrosis*

To validate Dt81Hepa1–6 cells as a suitable cell line for HCC development, we first compared gene expression levels of Dt81Hepa1–6 cells to primary murine hepatocytes via RNA sequencing (RNAseq). HCC key genes *Mcm3*, *Spats2*, and *Mcm6* and *Nt5dc2* [32], were significantly upregulated compared to healthy hepatocytes (Fig. 1A). Based on the SMITH LIVER CANCER gene set, Dt81Hepa1–6 were closer to human HCC than to primary murine hepatocytes (Fig. S8A). Since we observed a notable increase in the upregulation of alpha-fetoprotein gene (*Afp*), a standard clinical marker for HCC diagnosis [33], we tested its expression at the protein level *in vitro*. AFP levels were found to be increased in the supernatant of HCC cells (Dt81Hepa1–6) and absent in non-malignant cells (MHSC-SV40 hepatic stellate cells, AML-12 hepatocytes, NIH/3T3 fibroblasts, SVEC4–10 endothelial cells, RAW 264.7 macrophages or DC2.4 dendritic cells) or non-HCC cancer cells (B16/F10 melanoma cells) (Fig. 1B). Notably, AFP levels correlated with the cell number ($R^2 = 0.95$), suggesting AFP as a surrogate marker for tumor load *in vivo* (Fig. 1C).

For tumor cell inoculation, Dt81Hepa1–6 cells were injected into the spleen of 6–8 week-old wildtype C75BL/6 mice [23]. Following injection, cells reseeded to the liver via the portal vein. Four weeks post intrasplenic injection, mice were sacrificed, and tumor-bearing livers were harvested (**Model 1: HCC;** Fig. 1D). We expanded this model to mimic the development of HCC in cirrhotic livers. To develop advanced fibrosis/early cirrhosis in the liver (**Model 2: cirrhotic HCC (C-HCC);** Fig. 1D), mice were gavaged with fibrogenic CCl_4 for 6 weeks before tumor cell inoculation. A rest phase of one week was introduced to avoid injection of cancer cells in an acute inflamed liver, triggered by CCl_4 exposition. Two additional groups (healthy and cirrhotic) were added as controls (Fig. 1D).

To evaluate the development of malignant lesions, the livers of all groups (healthy, cirrhotic, HCC, and C-HCC) were weighed and serum AFP levels were determined. At sacrifice, multiple macroscopic lesions were visible in the livers of tumor-bearing mice (Fig. 1E), while only small lesions were observed at the puncture site in the spleen (Fig. S8B). After 4 weeks, livers from both, HCC and C-HCC groups showed a substantial increase in weight in comparison to healthy or cirrhotic control groups. A slight increase in liver weight was observed in cirrhotic livers, as compared to healthy livers (1.5 g healthy vs. 1.7 g cirrhotic), which is

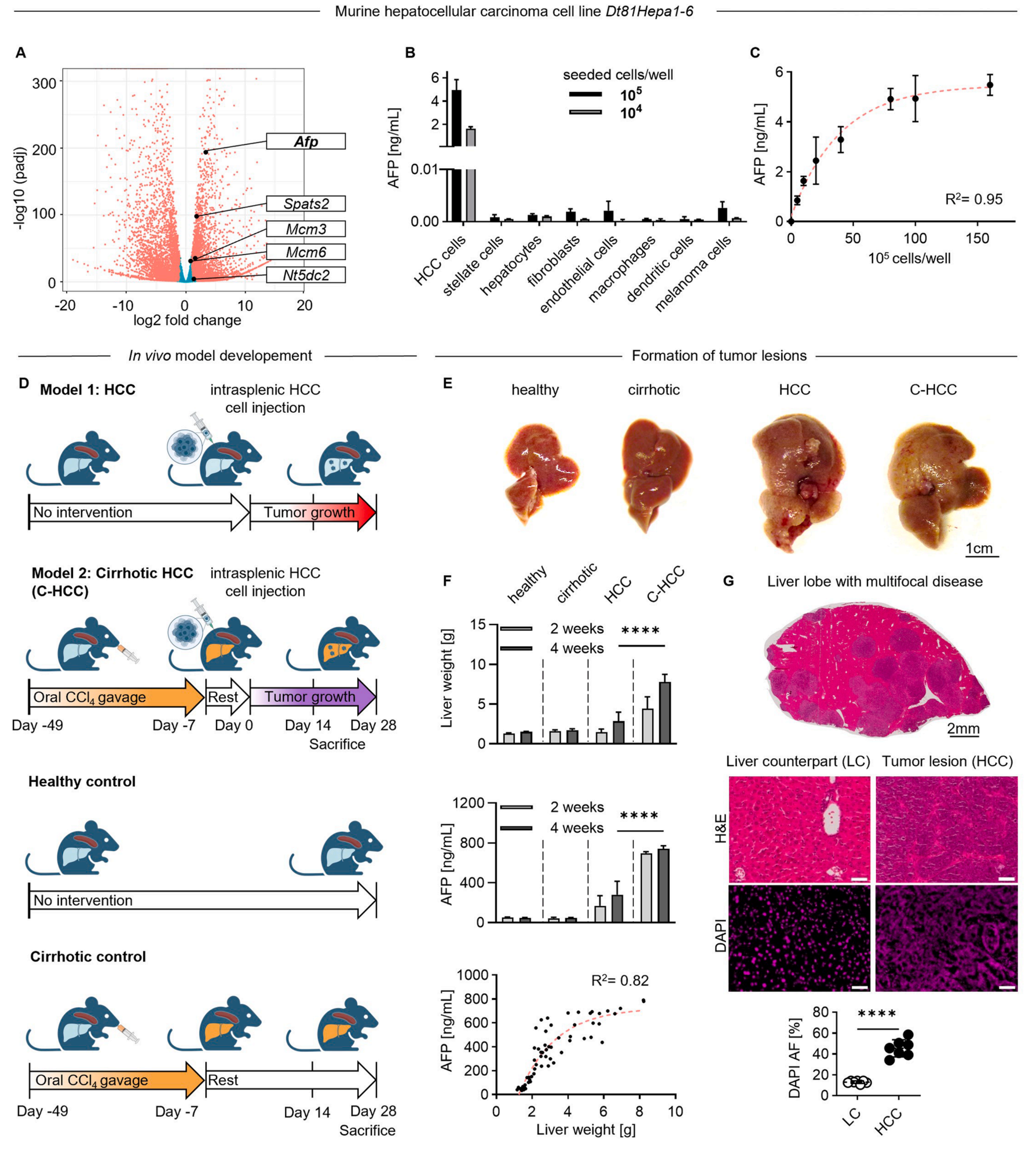

Fig. 1. Development of a hepatocellular carcinoma model with and without parenchymal liver damage in immunocompetent mice. (A) RNA-Seq analysis of HCC cells (Dt81Hepa1–6) revealed significant upregulation of human HCC key genes. (B) Quantification of AFP in cell culture supernatants of Dt81Hepa1–6 cells, hepatocytes as well as other (non)-malignant cells following 48 h incubation. AFP was exclusively detected in Dt81Hepa1–6 cells. (C) AFP correlated with the seeded HCC cell density. (D) Experimental outline of animal model development based on intrasplenic injection of Dt81Hepa1–6 cells. For additional induction of advanced fibrosis/early cirrhosis, mice were gavaged with CCl_4 for 6 weeks. A rest phase of 1 week prevented the injection of cells in acute inflamed livers. As controls, healthy mice or mice treated with CCl_4 alone followed by a resting phase of 5 weeks were used. Livers were harvested at 11 weeks post-experimental initiation. (E) Images of extracted livers from non-tumor and tumor-bearing mice. (F) Liver weights and serum AFP levels as measured in healthy and cirrhotic controls as well as HCC and C-HCC mice. Formation of malignant tumor lesions led to a substantial increase in liver weight and AFP levels; n = 3–4. Concentration of serum AFP correlated with liver weight; n = 65. (G) H&E staining of whole liver lobes revealed the difference between tumor lesions and the adjacent liver counterpart (LC), where the former is depicted as a high-cell density round structure. Cell density, determined by DAPI staining and area quantification, showed tumor regions to have a significantly higher cell density as compared to the adjacent LC; n = 7. Scale bar = 50 µm, AF = area fraction, LC = liver counterpart, C = cirrhotic, Statistical significance: ****$P < 0.0001$, ***$P < 0.001$, **$P < 0.01$, *$P < 0.05$.

attributed to the fibrosis induction [17]. Similarly, serum AFP levels of tumor-bearing mice were substantially elevated in comparison to tumor-free mice (Fig. 1F). Serum AFP levels of cirrhotic and healthy liver-bearing mice were comparable (49 ng/mL healthy vs. 50 ng/mL cirrhosis), demonstrating that AFP is not an indicator of cirrhosis, and thus serves as an effective marker for tumor-burden. Most importantly, C-HCC mice had a significantly higher tumor load than non-cirrhotic HCC mice, as evidenced by higher liver weights (2.6-fold; $^{****}P < 0.0001$) and higher serum AFP levels (2.7-fold; $^{****}P < 0.0001$) indicating that livers with parenchymal damage are more susceptible to tumor growth. The model consistency was further supported by a positive correlation between liver weight (a proxy for tumor burden) and serum AFP concentration ($R^2 = 0.82$) (Fig. 1F). Moreover, apart from a cell concentration of $5\cdot10^5$ per mouse for tumor

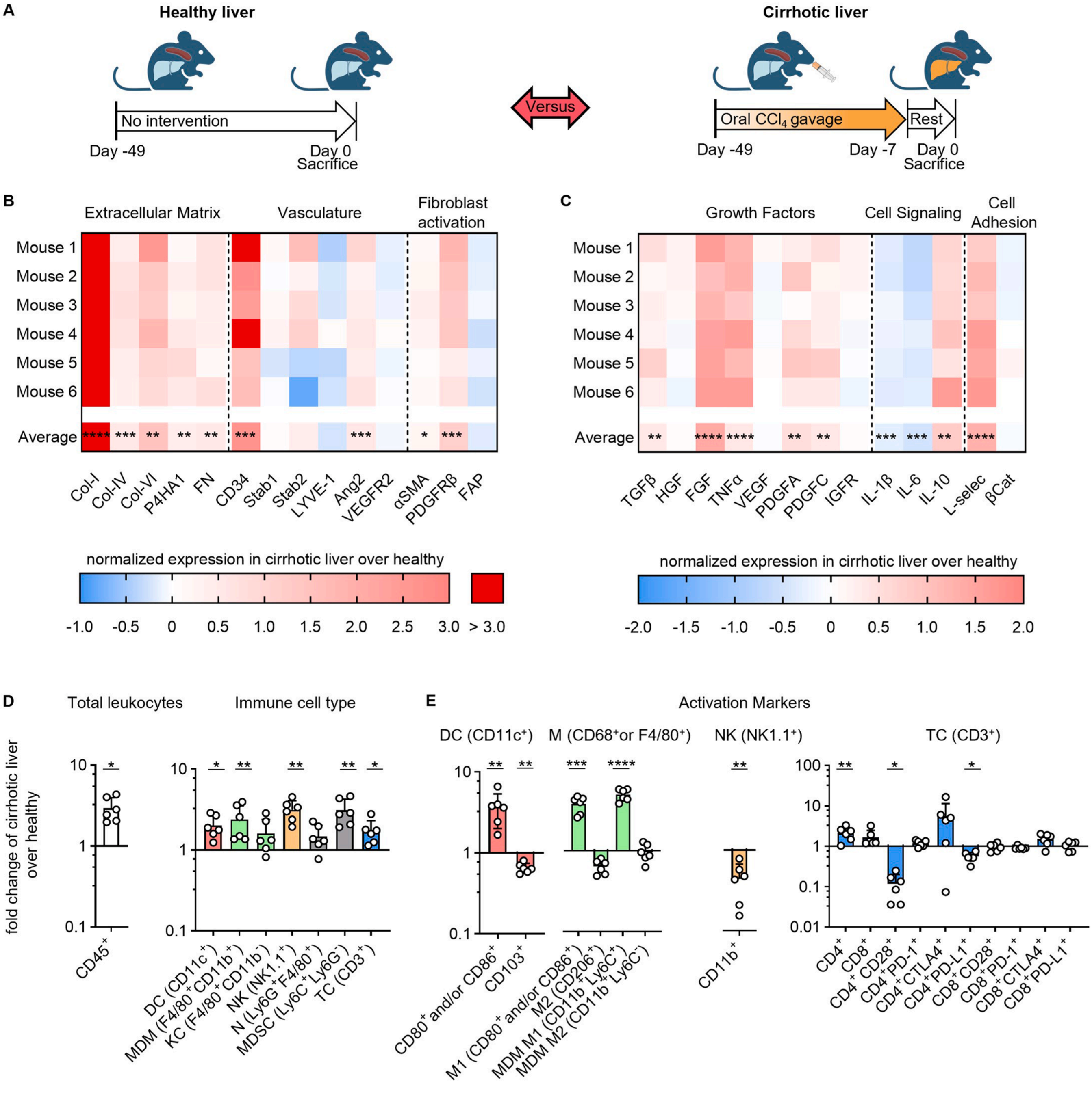

Fig. 2. CCl_4-induced cirrhosis creates a tumor-promoting microenvironment through production of growth stimulating proteins and cytokines, as well as immune cell deactivation. (A) The liver microenvironment of healthy and cirrhotic liver mice was analyzed right before Dt81Hepa1–6 inoculation. (B-C) RT-qPCR analysis of cirrhotic *vs.* healthy livers. Cirrhotic livers displayed substantial upregulated expression of genes involved in ECM deposition, vascularization, and fibroblast activation. An increase of growth factors was additionally observed in cirrhotic livers. Lower levels of inflammatory cytokines and simultaneously increased levels of anti-inflammatory cytokines together indicated decrease of the acute inflammatory phase, which was induced by CCl_4 administration. Adhesion molecules, involved in immune cell rolling, were also upregulated. (D-E) Immune cell infiltration is increased in cirrhotic livers as assessed by flow cytometry. However, the expression of activation markers revealed that the present immune cells had a rather patrolling than phagocytic profiles which were favorable for tumor growth. RT-qPCR and flow cytometry results are shown as relative change normalized to healthy controls. DC = dendritic cell, MDM = monocyte-derived macrophage, KC = Kupffer cell, NK = natural killer cell, N = neutrophil, MDSC = myeloid-derived suppressor cell, TC = T cell, M = macrophage. Statistical significance: $^{****}P < 0.0001$, $^{***}P < 0.001$, $^{**}P < 0.01$, $^{*}P < 0.05$; n = 6.

inoculation, two additional concentrations were examined. Across all concentrations a consistently elevated tumor burden was observed in cirrhotic livers compared to healthy livers, confirming the hypothesis that continuous CCl_4 administration results in accelerated tumor progression (Fig. S8C). Finally, microscopic tumors were visualized with haematoxylin and eosin (H&E) staining, allowing precise discrimination of tumor lesions (dark-stained round structures) and non-malignant (light-stained) liver counterpart (LC). Similarly, in DAPI-stained fluorescence microscopy images the tumor regions displayed a significantly higher cell density in comparison to non-malignant LC (3.5-fold; $^{****}P < 0.0001$; Fig. 1G). Compared to human HCC, the growth pattern identified in this model is less trabecular,hence, shares similarities to adenocarcinoma, a second type of primary liver cancer, but the multifocal nodded phenotype and the genomic profile clearly categorize it as HCC (Fig. 1A,G) [34].

3.2. *Cirrhotic livers display pro-tumorigenic pathological changes*

To examine the pathophysiological differences that accelerate tumor growth in cirrhotic livers, we harvested livers from healthy and cirrhotic mice right before they would undergo intrasplenic injection of HCC cells (Fig. 2A). RT-qPCR results revealed significantly increased expression of various genes related to fibrotic manifestation in cirrhotic *vs.* healthy livers (Fig. 2B, Fig. S9). An excessive ECM deposition can provide physical and biochemical cues to promote cancer cell invasion, migration, and lastly, proliferation [35–37]. On top, we observed an increase of CD34 and collagen IV (Col-IV) expression in cirrhotic livers (Fig. 2B, Fig. S9), which indicated capillarization of liver sinusoids upon cirrhosis induction. Capillarization is characterized by the loss of sinusoidal fenestrations and the formation of a basal lamina [38,39]. In healthy livers, liver sinusoids are highly fenestrated to enable the free exchange of substances between flowing blood and the liver cells. The phenotypic switch of vessels observed in cirrhotic livers can lead to reduced blood flow, which results in a decreased delivery of oxygen and nutrients to the liver cells, thus creating a hypoxic microenvironment [40]. Hypoxia, in turn, is known to promote tumor cell survival, growth, and progression, as well as tumor angiogenesis [41]. Additionally, a functional study using angiogenesis-targeting RNA interference (RNAi), demonstrated the relevance of angiogenesis for the tumor growth in this model [42].

A similar pattern was also observed for several growth factors that were found upregulated in cirrhotic mice (Fig. 2C, Fig. S10). By binding to the surface of tumor cells, growth factors can stimulate their proliferation [43]. Finally, due to the one week of interruption of CCl_4 administration, we achieved the elimination of the acute inflammatory phase, evidenced by low inflammatory cytokine levels of IL-1β and IL-6 levels, and the upregulation of anti-inflammatory cytokine IL-10 (Fig. 2C, Fig. S10). This allows the inoculation of HCC cells in a non-acute inflammation environment, resembling the non-acute inflammatory status of cirrhosis patients with beginning HCC [44]. Lastly, L-selectin (L-selec) was found to be significantly upregulated in cirrhotic livers. L-selec, an adhesion molecule, is usually found in leukocytes and mediates their initial adhesion to endothelial cells during an inflammatory response [45]. Likewise, cancer cells can use this mechanism to facilitate extravasation from the bloodstream to their targeted tissue, which has been observed in cancer metastasis [46].

Following the cytokine and growth factor profiling, we set out to identify changes in the cellular composition of cirrhotic and healthy livers. The total amount of $CD45^+$ leukocytes was increased 3-fold after CCl_4 administration. Among these, both myeloid and lymphoid cells were highly present (Fig. 2D, Fig. S11A). In cirrhotic livers, dendritic cells (DC) exhibited a distinct expression profile with upregulation of CD80 (B7–1) and CD86 (B7–2), and downregulation of CD103 (ITGAE) expression (Fig. 2E, Fig. S11B). The observed alterations in expression levels suggest that these cells were engaged in a patrolling rather than a phagocytic role within the cirrhotic livers, which in turn facilitates tumor growth [47]. Similar trends were seen for macrophages. $CD80^+$, $CD86^+$ as well as $Ly6C^+$ (on monocyte-derived macrophages, MDM) are predominantly expressed in pro-inflammatory, pro-fibrogenic M1 type macrophages, while $CD206^+$ and $Ly6C^-$, respectively, can indicate the presence of anti-inflammatory, anti-fibrogenic M2 macrophages [48]. In cirrhotic livers, an increased infiltration of M1 macrophages was observed, while no difference was seen in the abundance of M2 macrophages in healthy *vs.* cirrhotic livers (Fig. 2E, Fig. S11C). This pattern indicated sustained inflammation and fibrosis in the cirrhotic livers [49,50]. Additionally, a decrease in phagocytic $CD11b^+$ NK cells and an increase in $CD11b^-$ NK cells were observed in cirrhotic livers (Fig. 2E, Fig. S11D). Lastly, we noticed a higher presence of $CD4^+$ helper T cells and cytotoxic $CD8^+$ T cells in the cirrhotic livers as compared to the healthy livers (Fig. 2E, Fig. S11E).

In addition to regular cell markers, expression of co-stimulatory receptor CD28 and immune checkpoint receptors CTLA-4 and PD-1 were analyzed for both $CD8^+$ and $CD4^+$ T cells (Fig. 2E, Fig. S11E). While CD28 is crucial for T cell activation, CTLA-4 competes with CD28 for binding to B7 ligands and inhibits T cell activation [51]. For $CD4^+$ T cells the simultaneous downregulation of CD28 and upregulation of CTLA-4 suggested a regulatory or tolerogenic response to the inflammatory environment in cirrhotic livers. This could be a mechanism to prevent further T cell activation, mitigate inflammation, and avoid further tissue damage and the progression of cirrhosis [52]. A similar trend was observed for $CD8^+$ T cells.

To summarize, upon cirrhosis induction, we observed an increase in patrolling but decrease in phagocytic monocyte subpopulations. Patrolling monocytes capture, process and present antigens. They activate T cells, to initiate targeted immune responses towards cancer cells. However, T cell activation is dampened through the CTLA-4/PD-1 axis, therefore hindering efficient antigen presentation and cancer cell recognition which is favorable for HCC cell growth. Importantly our findings suggested a fibrotic and growth-stimulating liver microenvironment upon CCl_4-induced cirrhosis, favorable for homing and proliferation of injected HCC cells.

3.3. *HCC lesions display an extensive desmoplastic reaction*

The alteration of the ECM in the HCC and C-HCC lesions was analyzed and compared to their adjacent non-malignant LC. The total collagen content was determined via a hydroxyproline (HYP) assay. This test allows for the detection of the post-translational modification of the amino acid proline, which is only present in collagen [53]. We found that the C-HCC model contains the highest amounts of collagen in comparison to the healthy liver (19-fold; $^{****}P < 0.0001$), to the cirrhotic liver (4-fold; $^{****}P < 0.0001$), and the HCC model (3-fold; $^{****}P < 0.0001$) (Fig. 3A). The later observation correlates with the observed increased tumor burden in the C-HCC as compared to HCC model. Next, we performed extensive histological analysis. Sirius red staining corroborated the presence of a dense stroma in tumors, revealing multifocal disease where nodules are distinctively separated from the surrounding liver tissue (Fig. 3B). Morphometric collagen quantification of Sirius Red-stained liver sections revealed that tumor lesions displayed a significant increase in collagen content in comparison to the adjacent LC (5- to 19-fold; $^{****}P < 0.0001$; Fig. 3C). Importantly, the C-LC displayed a significantly increased collagen area as compared to LC (3.5-fold; $^{***}P = 0.0002$), which confirms the successful cirrhosis induction in the model prior to tumor cell inoculation. The cirrhosis induction was further seen in cirrhotic control livers as compared to healthy control livers (Fig. S12A,**B**).

The ECM components Col-I, Col-IV, and fibronectin (FN) were significantly higher expressed in tumor tissues compared to LC and C-LC (6- to 16-fold for Col-I: $^{****}P < 0.0001$; 2- to 4-fold for Col-IV: $^{****}P_{LC\ vs.\ HCC} < 0.0001$, $^{**}P_{C\text{-}LC\ vs.\ C\text{-}HCC} = 0.0065$; 2- to 4-fold for FN: $^{****}P_{LC\ vs.\ HCC} < 0.0001$, $^{***}P_{C\text{-}LC\ vs.\ C\text{-}HCC} = 0.0005$; Fig. 3D). Surprisingly, Col-IV was decreased in the tumor lesions of C-HCC, compared to HCC (0.7-fold; $^{*}P = 0.0225$). Col-IV is usually found in the basal lamina which

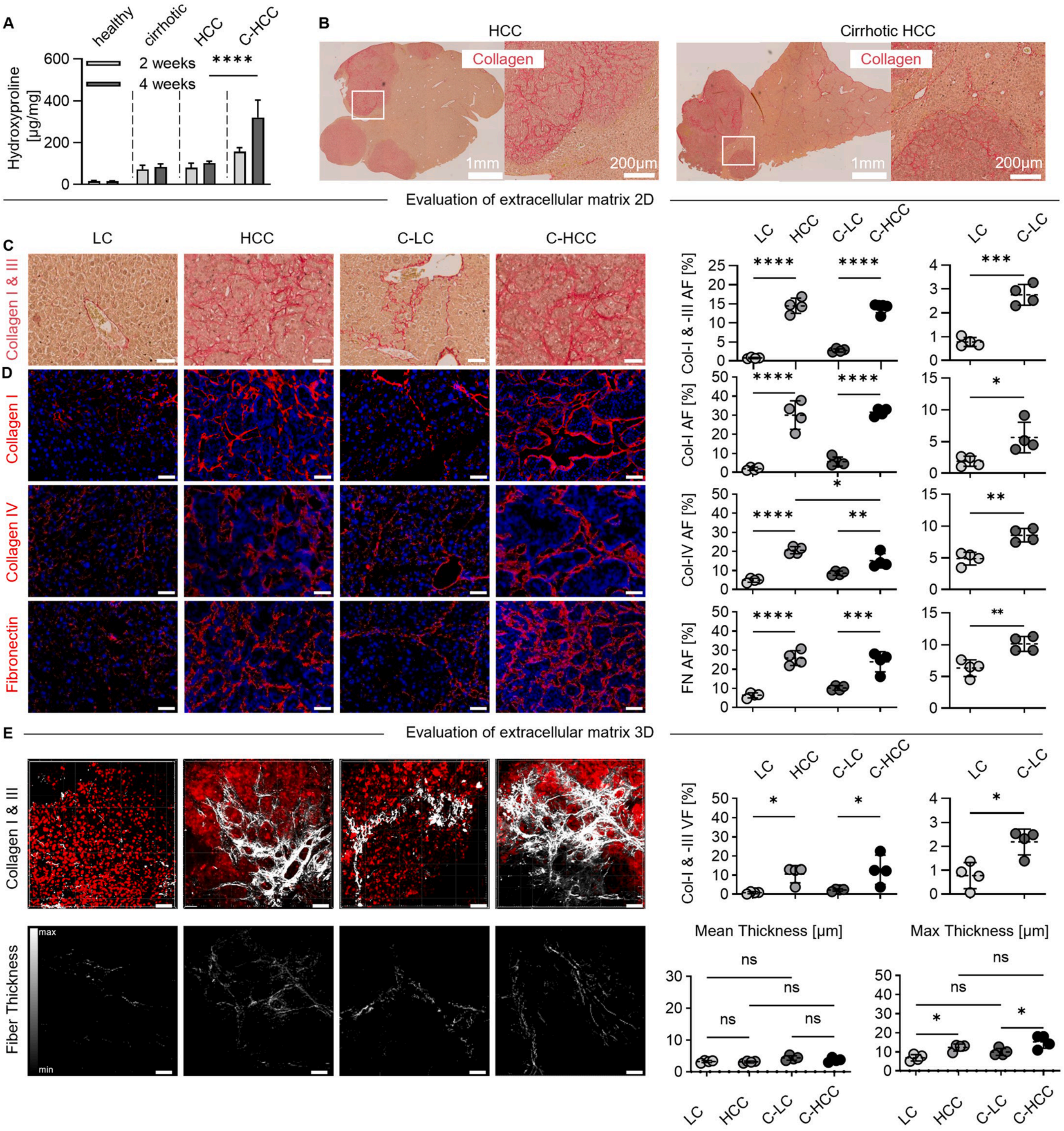

Fig. 3. CCl_4-induced cirrhotic liver and HCC nodules are characterized by strong ECM multi-component deposition. (A) Total liver collagen content was assessed via the hydroxyproline (HYP) assay. C-HCC and HCC samples displayed increased HYP content, alluding to the high collagen content within these lesions. (B) Sirius Red staining for collagen visualization. Tumors can be visibly separated by the LC due to the presence of a dense ECM in the former. (C) Representative histological sections stained for total collagen (Sirius Red). The analyses confirmed successful fibrosis induction prior to the HCC cell inoculation. Furthermore, both HCC and C-HCC tumors displayed significant collagen increase in comparison to their respective LC. (D) Representative histological sections stained for Col-I, Col-IV, and fibronectin confirmed their increased expression within the tumor lesions. In addition, C-LC displayed fiber-like structures in the liver parenchyma, which, together with the respective quantification, indicated an elevated ECM deposition in the LC of the C-HCC model as compared to the LC of the HCC model. (E) TPLSM images exemplify a significantly higher total collagen volume density in HCC and C-HCC tumors as compared to their respective LC. The C-LC again showed higher deposition of ECM as compared to the non-cirrhotic LC. Finally, while collagen mean fiber thickness remained similar for all groups, collagen max fiber thickness was significantly higher in both tumor models. Scale bar = 50 µm, AF = Area fraction, VF = volume fraction, LC = liver counterpart, HCC = hepatocellular carcinoma, C = cirrhotic. Statistical significance: $^{****}P < 0.0001$, $^{***}P < 0.001$, $^{**}P < 0.01$, $^{*}P < 0.05$, $^{ns}P > 0.05$ (not significant); n = 3–4.

also covers vasculature. The disruption of the basal lamina in C-HCC is associated with the invasive and metastatic behavior of the cancer cells. The breakdown of the basal lamina allows cancer cells to penetrate the surrounding tissue, enter blood vessels, and spread to distant sites in the body, thereby contributing to the aggressiveness of the disease [54]. Finally, we observed increased deposition of ECM components in the C-LC as compared to LC (2- to 3-fold; for Col-I: $*P = 0.0246$; for Col-IV: $**P = 0.0024$; for FN $**P = 0.0047$; Fig. 3D). These differences were similarly seen in healthy vs. cirrhotic control livers (Fig. S12C).

Above-described trends were observed also upon quantification of collagen volumes via two-photon laser scanning microscope (TPLSM). Collagen volume within the tumor lesions were 4- to 20-fold higher compared to LC ($*P_{LC\ vs.\ HCC} = 0.0414$; $*P_{C\text{-}LC\ vs.\ C\text{-}HCC} = 0.0262$; Fig. 3E). Additionally, collagen volume in the C-LC was higher as compared to the LC (2-fold; $*P = 0.0106$). This trend was further confirmed in the comparison between the non-tumor-bearing healthy livers and non-tumor-bearing cirrhotic livers (Fig. S12D). Tumor lesions also displayed higher maximum fiber thickness in comparison to their respective LC (1.6-fold; $*P_{LC\ vs.\ HCC} = 0.0310$; $*P_{C\text{-}LC\ vs.\ C\text{-}HCC} = 0.0304$; Fig. 3E). Thicker fibers lead to increased stiffness, contributing to the desmoplastic TME in HCC. All above-mentioned trends were confirmed via PCR analysis (Fig. S13).

Finally, we analyzed the progression of fibrosis during tumor development in the adjacent LC and inside the tumor lesions. First, we compared collagen content of adjacent (C-)LC after 4 weeks of tumor growth with collagen levels from healthy and cirrhotic livers right

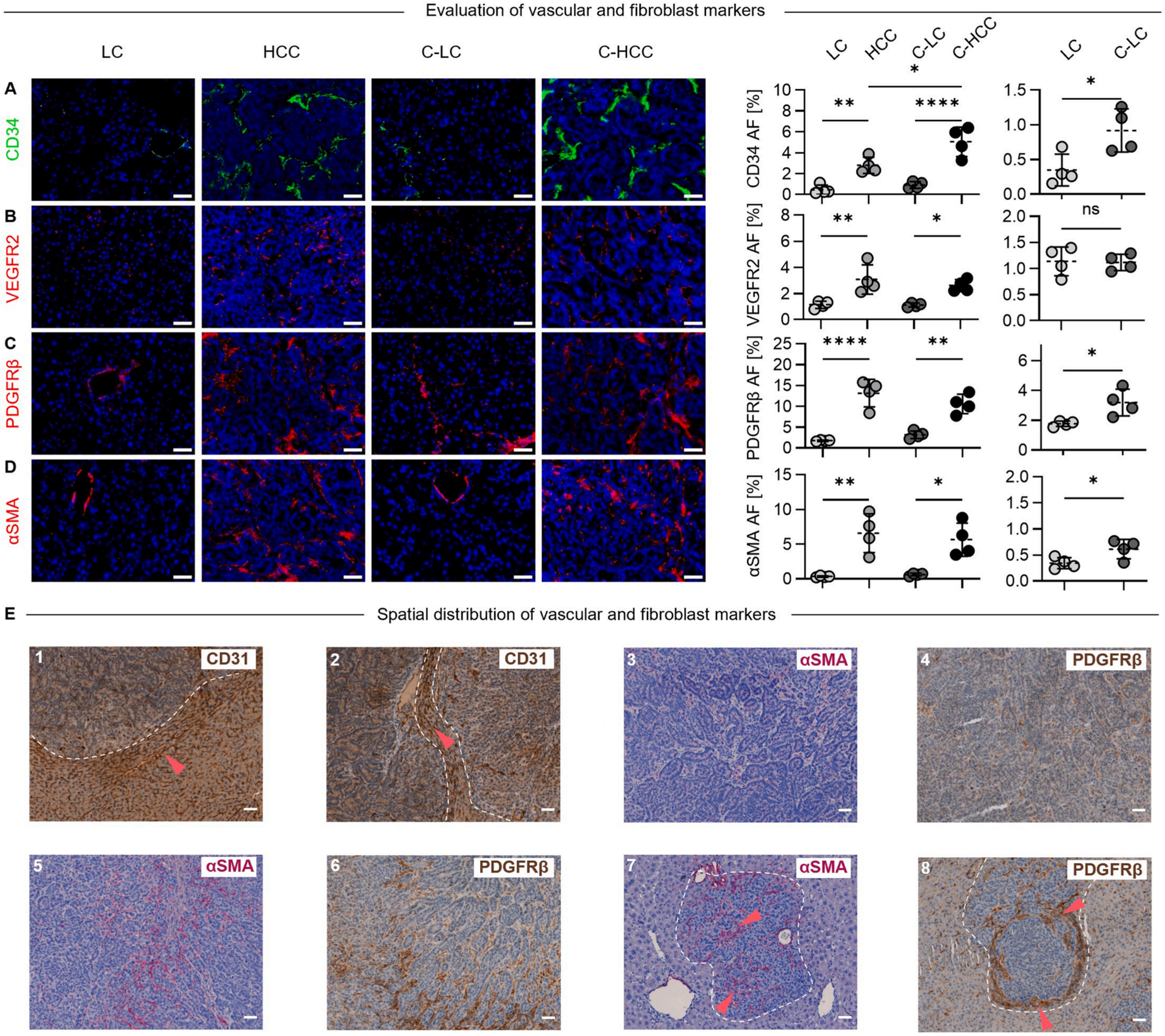

Fig. 4. C-HCC and HCC tumors display high vascularization and fibrogenic activity. (A-B) Representative histological sections stained for vascularization. CD34 (capillary endothelial cells) and VEGFR2 are upregulated in C-HCC and HCC lesions, indicating high vascularization and angiogenesis. (C-D) Representative histological sections stained for activated (cancer-associated) fibroblasts. Quantification of PDGFRβ and αSMA indicated high expression in tumor areas as compared to (C-)LC. In C-LC, significantly higher expression of PDGFRβ indicates the activated state of liver fibroblasts. (E) Representative histological sections stained for CD31, αSMA, and PDGFRβ. Image 1–2: CD31 staining indicates hepatic vessels to be compressed between highly proliferating tumor tissue and LC, indicative that tumors grow with pushing borders. Image 3–6: Highly heterogenous expression of αSMA and PDGFRβ throughout the tumor tissue indicates spatial CAF activation. Image 7–8: PDGFRβ and αSMA show high expression in and around small tumor nodules. Scale bar = 50 µm, AF = area fraction, LC = liver counterpart, HCC = hepatocellular carcinoma, C = cirrhotic. Statistical significance: $****P < 0.0001$, $***P < 0.001$, $**P < 0.01$, $*P < 0.05$, $^{ns}P > 0.05$ (not significant); n = 3–4.

before potential HCC cell injection. The results showed that the collagen content was similar at time of HCC cell injection and 4 weeks after tumor growth in the non-malignant parts of the liver (Fig. S14A). This shows that the protocol used to establish cirrhosis guarantees a sufficient grade of fibrosis/cirrhosis during tumor growth. Interestingly, desmoplasia inside tumors was increased over-time, which was evident when comparing Col-I, Col-IV and FN contents from HCC tumors between 2 weeks vs. 4 weeks after HCC cell inoculation (Fig. S14B,C). This is well in line with the fact that advanced stage cancers are more desmoplastic [55,56].

Altogether, it is evident that the CCl_4 administration induced stable advanced fibrosis/early cirrhosis in the C-HCC livers and cirrhotic control livers, leading to significant alterations in the ECM. ECM components were highly abundant and homogeneously distributed within tumor lesions, creating a highly desmoplastic and pro-tumorigenic environment.

3.4. Liver tumors induce angiogenesis and are strongly vascularized

Next, the expression of vascular and fibroblast markers in the tumors and adjacent LC was analyzed in detail. CD34 is a marker for endothelial cells and can be used to visualize abnormal tumor vasculature, as well as portal veins and sinusoidal capillarization in the liver, VEGFR2 indicates neovascularization and angiogenesis [57,58]. Both markers were found to be significantly overexpressed in tumor tissues compared to their adjacent (C-)LC (2- to 6-fold; for CD34: $^{**}P_{LC\ vs\ HCC} = 0.0096$ and $^{****}P_{C\text{-}LC\ vs\ C\text{-}HCC} < 0.0001$, for VEGFR2: $^{**}P_{LC\ vs\ HCC} = 0.0043$ and $^{*}P_{C\text{-}LC\ vs\ C\text{-}HCC} = 0.0253$; Fig. 4A,B). Hypervascularization and increased angiogenesis are hallmarks of HCC and essential for supplying the growing tumor with nutrients and oxygen [59]. Interestingly, tumor lesions from C-HCC showed increased vascularization compared to tumor tissue from HCC (1.8-fold; $^{*}P = 0.0124$) which correlates with the increased tumor growth and aggressiveness in this model. An increase in CD34 was also observed in C-LC compared to the LC of HCC (2-fold; $^{*}P = 0.0254$; Fig. 4A,B), indicating sinusoidal capillarization in cirrhosis. Similar trends were observed for cirrhotic control tissues as compared to healthy controls (Fig. S15A).

Smooth muscle actin (αSMA) and platelet-derived growth factor receptor (PDGFRβ) are usually found on pericytes surrounding the vasculature but are also expressed by activated HSC and activated CAF [13,60]. Both fibroblast markers were majorly upregulated in tumor tissues (3- to 7-fold for PDGFRβ; $^{****}P_{LC\ vs.\ HCC} < 0.0001$ and $^{**}P_{C\text{-}LC\ vs.\ C\text{-}HCC} = 0.0014$; 9- to 19-fold for αSMA; $^{**}P_{LC\ vs.\ HCC} = 0.0022$ and $^{*}P_{C\text{-}LC\ vs.\ C\text{-}HCC} = 0.0106$; Fig. 4C,D). The high expression in tumors indicated high CAF prevalence. CAF support tumor growth, invasion, and metastasis through ECM remodeling, cytokine secretion, and elevation of angiogenesis, and therefore contribute to the aggressiveness of the HCC models [13]. PDGFRβ was additionally found to be significantly upregulated in C-LC compared to LC (2-fold; $^{*}P = 0.0212$; Fig. 4C). Similar results were found for the comparison between healthy and cirrhotic control livers (Fig. S15B). In both LC and C-LC, αSMA was predominantly found on portal veins (Fig. 4D), a pattern similarly seen in healthy and cirrhotic control livers (Fig. S15B). The total expression level in cirrhotic control livers and C-LC was slightly higher compared to healthy livers and LC, respectively (Fig. 4D, Fig. S15B). This confirms the activation of fibroblasts and successful fibrosis development through CCl_4 gavage. Comparing αSMA expression of adjacent (C)-LC after 4 weeks of tumor growth with αSMA levels from healthy and cirrhotic livers right before potential HCC cell injection, no discernible difference was found. Nevertheless, it was revealed that in the C-LC, fibroblasts remained in an activated state, which is crucial in cirrhosis (Fig. S15C). RT-qPCR results confirmed all above-mentioned trends (Fig. S13).

In addition to the quantification of the various markers, their spatial distribution was examined. Liver tumor lesions exhibited a growth pattern characterized by a pushing border, as evidenced by compressions of adjacent liver sinusoids (Fig. 4E**; image 1–2**). Additionally, qualitative analysis demonstrated heterogeneous expression patterns of αSMA and PDGFRβ, with low (Fig. 4E**; image 3–4**) and high expression regions (Fig. 4**E; image 5–6**). Finally, some tumors were organized in small lesions, separated from the surrounding LC. In those lesions, it can be clearly seen that the expression of αSMA and PDGFRβ is enhanced within the lesion borders (Fig. 4E**; image 7–8**).

Lastly, the levels of hypoxia were determined, as hypoxia is a driver of angiogenesis [61]. To demonstrate a correlation between hypoxia and angiogenesis in our model, we stained for hypoxia-inducible factor 1-alpha (HIF1α), a transcription factor that regulates cellular responses to low oxygen levels, promoting adaptation by activating genes involved in angiogenesis, metabolism, and survival. It was identified that in (C-) HCC tumor lesions, HIF1α is heterogeneously expressed (Fig. S16A), however substantially elevated as compared to adjacent (C-)LC (Fig. S16B).

In summary, tumors are characterized by an enhanced blood supply, amongst other triggered by hypoxia, and a supportive stromal environment, which enhances cancer growth and tumor progression and is associated with more aggressive and advanced stage malignancy.

3.5. (C-)HCC-bearing mice display increased infiltration of myeloid cells to the parenchyma and lymphoid immune cells to the tumor nodules

The immune cell composition of the tumor models was analyzed, focusing on the abundance of macrophages, neutrophils, cytotoxic T cells, and helper T cells as they represent important players for initiation and regulation of immunological reactions, but also drive tumor growth or recognize and destroy tumor cells. Macrophages ($CD68^+$) were found abundantly in the tumor tissue but in higher frequencies in the LC as compared to tumors (1.5- to 1.8-fold; $^{*}P_{LC\ vs.\ HCC} = 0.0286$, $^{***}P_{C\text{-}LC\ vs.\ C\text{-}HCC} = 0.0007$; Fig. 5A). This is in line with literature, showing that macrophage accumulation is decreased in HCC regions as compared to the surrounding tissue [62]. Moreover, even in a healthy state, the liver typically contains a large population of liver-specific macrophages [48]. Additionally, CD68 expression in the LC and C-LC was slightly higher compared to non-tumor-bearing healthy and cirrhotic control livers (1.3-fold; $^{*}P_{healthy\ vs.\ LC} = 0.0259$ and $^{ns}P_{cirrhotic\ vs.\ C\text{-}LC} = 0.1436$; Fig. S17A**)**. An increase in CD68 area fraction was also observed in cirrhotic control livers as compared to healthy control livers (Fig. S17A). In the C-LC, as well as cirrhotic controls, infiltrating monocyte-derived macrophages could be differentiated from resident Kupffer cells by their circular shape. This is well in line with our previous results demonstrating increased macrophage presence in cirrhotic livers majorly due to increased infiltration of monocyte-derived macrophages (Fig. 2D). In HCC, tumor-associated macrophages are often abundant and their occurrence correlates with lower recurrence-free survival and overall survival [63].

Similar patterns were observed for neutrophils ($Ly6G^+$). Inside tumor lesions, neutrophils were less abundant in comparison to the adjacent (C-)LC regions (3-fold; $^{****}P_{LC\ vs.\ HCC} < 0.0001$ and $^{***}P_{C\text{-}LC\ vs.\ C\text{-}HCC} = 0.0003$; Fig. 5B). However, the abundance of neutrophils in (C-) LC was significantly higher in comparison to non-tumor-bearing control livers, both for the non-cirrhotic and cirrhotic model (4–8-fold; $^{***}P_{healthy\ vs.\ LC} = 0.0001$ and $^{**}P_{cirrhotic\ vs.\ C\text{-}LC} = 0.023$; Fig. S17B). The fact that neutrophils were observed more in the adjacent LC rather than the lesion itself is not trivial, as neutrophils are major contributors to the extension of the tumor front [64]. Neutrophil-targeting therapies are currently entering clinical trials, as neutrophils are associated with poor prognosis [65].

Unlike myeloid cells, lymphoid cell abundancy was elevated in the tumor regions. Both helper ($CD4^+$) and cytotoxic ($CD8^+$) T cells were significantly more abundant in both HCC and C-HCC tumor regions as compared to their respective LC (1- to 2-fold; for CD4: $^{*}P_{LC\ vs.\ HCC} = 0.0141$ and $^{***}P_{C\text{-}HCC\ vs.\ C\text{-}LC} = 0.0004$; for CD8: $^{****}P_{LC\ vs.\ HCC} < 0.0001$ and $^{****}P_{C\text{-}}LC$ vs. C-HCC< 0.0001; Fig. 5C,D). Interestingly $CD4^+$ T cells were increased in C-HCC as compared to HCC (1.4-fold; $^{*}P = 0.0423$).

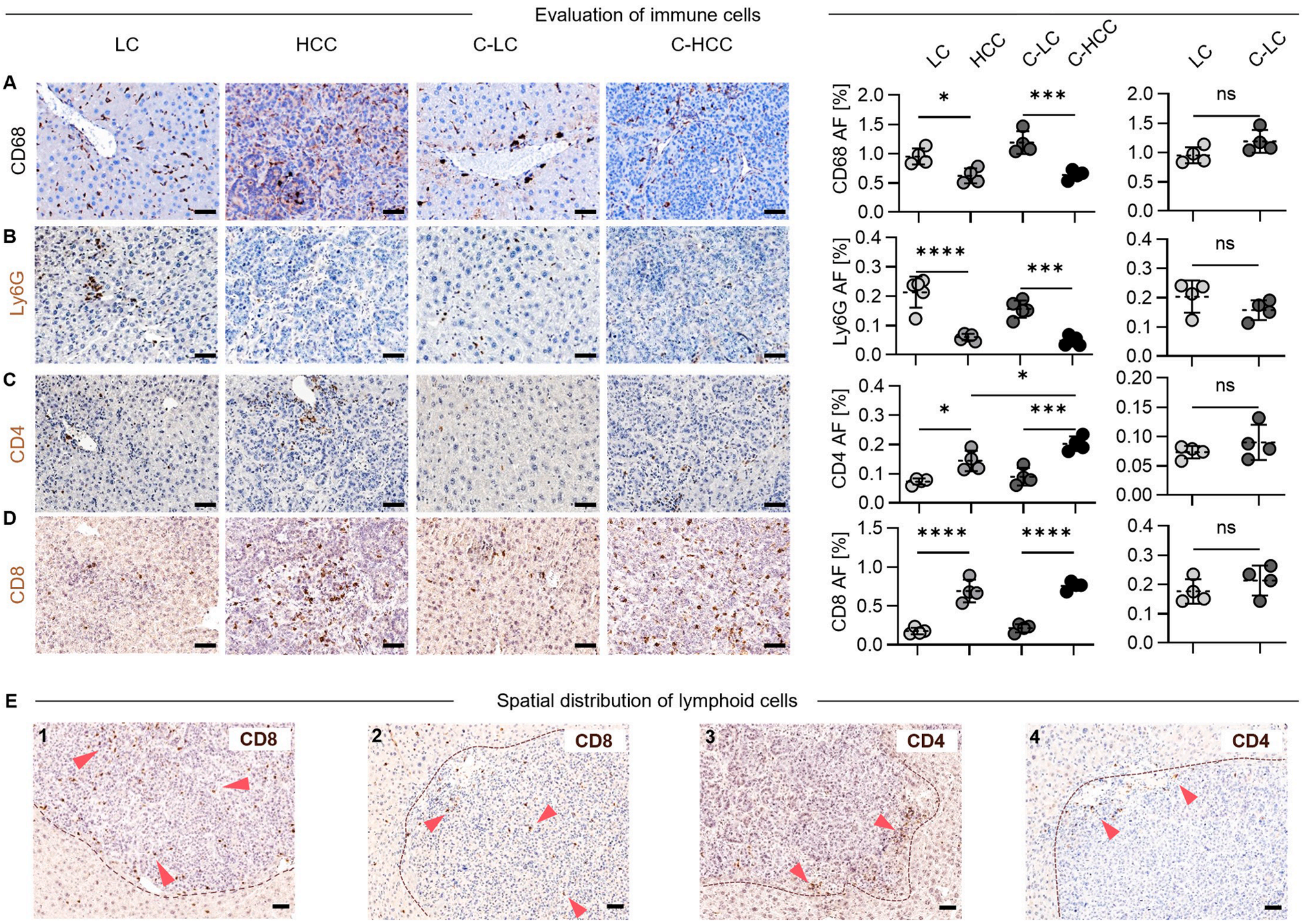

Fig. 5. C-HCC and HCC display increased numbers of myeloid cells in the liver parenchyma and of lymphoid cells in tumors. (A-B) The presence of macrophages ($CD68^{+}$) and neutrophils ($Ly6G^{+}$) is decreased inside tumors as compared to the (C-)LC. No differences were identified between LC and C-LC. (C-D) Helper T cells ($CD4^{+}$) and cytotoxic T cells ($CD8^{+}$) were found in high frequencies in tumor lesions. Again, no differences were identified between LC and C-LC. (E) Selected histological sections stained for CD4 and CD8. Cytotoxic T cells are well distributed in the tumor tissues, whereas helper T cells are mostly found in the periphery and intersection area between tumor lesions and (C-) LC. Scale bar = 50 µm, AF = area fraction, LC = liver counterpart, HCC = hepatocellular carcinoma, C = cirrhotic. Statistical significance: $^{****}P < 0.0001$, $^{***}P < 0.001$, $^{**}P < 0.01$, $^{*}P < 0.05$, $^{ns}P > 0.05$ (not significant); n = 3–4.

No significant difference was observed in helper T cell content in tumor-bearing livers in comparison to healthy and cirrhotic control livers (Fig. S17C). However cytotoxic T cells were found to be more abundant in tumor-bearing livers in comparison to healthy and cirrhotic control livers (2- to 5-fold; $^{**}P_{healthy\ vs.\ LC} = 0.0024$ and $^{*}P_{cirrhotic\ vs.\ C\text{-}LC} = 0.0148$; Fig. S17D). Taken together, these results indicate that the presence of tumors in both HCC and C-HCC models increased the expansion and infiltration of T cells to the tumor and LC, which usually takes place due to recognition of tumor-associated antigens and subsequent antigen presentation through antigen presenting cells. Despite high T cell infiltration, tumor growth is not inhibited which also indicated that T cells were in a non-activated state, and their function was compromised by tumors [51]. With respect to their spatial distribution, cytotoxic T cells were evenly distributed over the entire tumor lesion (Fig. 5E**; image 1–2**), while the $CD4^{+}$ T cells were more abundant in the periphery of the lesion or in the borders between the tumor lesion and the (C-) LC of (C-)HCC (Fig. 5E**; image 3–4**). Clinical studies have highlighted the diagnostic value of T cell populations in predicting HCC outcomes. Patients with higher CD4:CD8 ratios were observed to have a lower risk of recurrence, suggesting this immunological marker could be a valuable prognostic tool in post-transplant HCC management. In our model the ratio is 0.25 and therefore rather low. Low CD4:CD8 ratios are associated with higher risk of HCC development and indicate worse prognosis of disease [66–68].

Additionally, a functional analysis was performed to analyze immune activation in HCC-vs. C-HCC- bearing mice. In C-HCC tumors, DC showed an increased expression of co-stimulatory ligands B7–1/-2, which indicates enhanced antigen presentation and increased activation (Fig. S18). This increase in antigen presentation supports the differentiation and activation of cytotoxic T cells from their naïve to an effector or activated state and correlates with the chronic inflammatory state of the C-HCC model (Fig. S18). No differences were observed in macrophage polarization between the models, as macrophage polarization is primarily influenced by the tumor type and characteristics of the injected tumor cells [69]. Since these factors were similar in both models, macrophage polarization remained unchanged (Fig. S18).

In summary, the tumors drive the accumulation of myeloid and lymphoid immune cells not only to the tumors but also to the surrounding liver parenchyma.

3.6. HCC models show strong antitumor responsiveness to the first-line clinical therapy

In 2020, the IMbrave study showed that the combination of anti-PD-L1 (anti programmed cell death protein 1; atezolizumab) and anti-VEGF (anti vascular endothelial growth factor; bevacizumab), named Atezo-Bev, is superior to sorafenib in terms of overall and progression-free survival outcomes, thus it became the new first-line therapy [28].

Therefore, we challenged our murine model with AtezoBev to test its responsiveness to this therapeutic regimen (Fig. 6A). To be as close as possible to the clinical treatment, we chose an anti-PD-L1 antibody which features a variable region equivalent to atezolizumab (cross-reactive between human and mouse), which on top contains a constant region of mouse IgG1 [70]. In parallel we used bevacizumab which has been used in murine studies before [71]. It has been shown that bevacizumab and murine anti-VEGF had a similar effect on vascular reduction [72]. HCC and C-HCC mice received a total of three injections of AtezoBev, in body weight-adjusted doses (8 mg/kg), over three weeks. While untreated animals developed macroscopic tumors as described before, a complete remission appeared in the treated groups. Treated HCC and C-HCC mice showed non-elevated liver weights, comparable to those of healthy control mice (1.4 g for healthy control vs. 1.7 g for treated HCC and C-HCC; Fig. 6B). As AFP proved to be a quantitative tumor marker in our model, we measured the AFP levels in

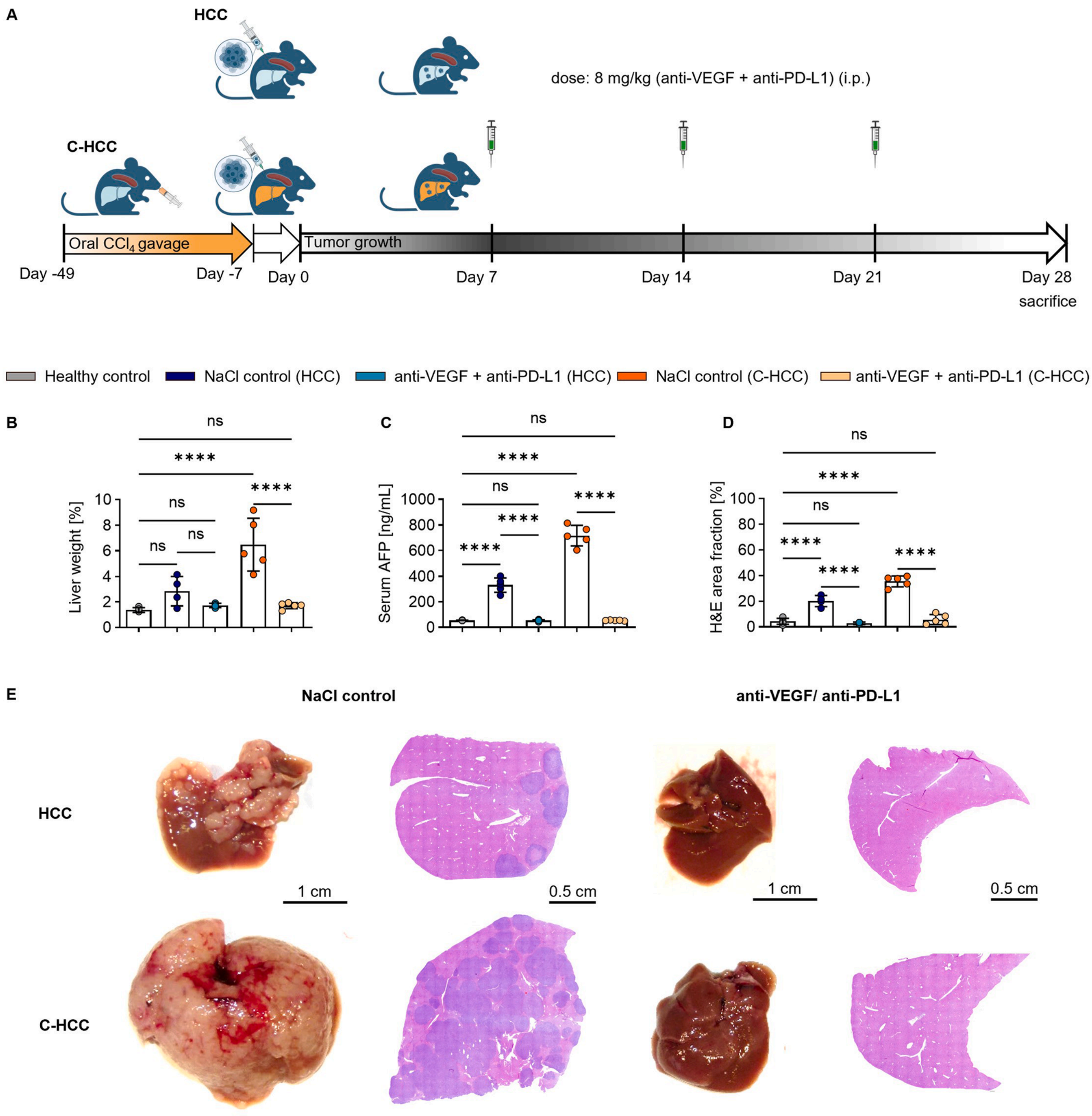

Fig. 6. Treatment with first-line anti-VEGF/anti-PD-L1 therapy results in a strong antitumor response in HCC and C-HCC tumor models. (A) Experimental outline for first-line therapy (AtezoBev) in C-HCC and HCC mice with bevacizumab (anti-VEGF) and an analogue of atezolizumab (anti-PD-L1). (B) Therapy resulted in a complete tumor remission at macroscopic level in both models as indicated by non-increased liver weight. (C) AFP was not increased following therapy, confirming tumor remission even on microscopic level. (D) In addition, H&E area fraction was not increased due to absence of tumor lesions. (E) Representative livers and H&E sections show the absence of malignant tumor lesions following therapy. Scale bar for liver images = 1 cm and for H&E images 0.5 cm respectively. C = liver counterpart, HCC = hepatocellular carcinoma, C = cirrhotic. Statistical significance: ****$P < 0.0001$, ***$P < 0.001$, **$P < 0.01$, *$P < 0.05$, $^{ns}P > 0.05$ (not significant); n = 5.

sera of (un-)treated HCC and C-HCC mice and controls. In AtezoBev-treated mice, AFP level dropped down to levels of healthy control mice (55 ng/mL for healthy control vs. 54 ng/mL for treated HCC and C-HCC; Fig. 6C). The tumor reductive effect was further confirmed via histological analysis of H&E-stained liver sections. No tumors were visually detected in neither of the HCC and C-HCC groups when treated with AtezoBev while tumors in non-treated groups were in the expected range ($^{****}P_{treated\ vs.\ untreated} < 0.0001$; Fig. 6D,E).

Taken together, our results indicate the robust responsiveness of the model to the standard clinical treatment. This can be explained by the high vascularization and relatively high abundance of $CD8^+$ T cells in the tumor tissue. Bevacizumab specifically binds to VEGF and therefore inhibits its binding to VEGFR2 receptors. This binding inhibition disrupts the signaling pathway that promotes angiogenesis and consequently reduces the formation of new blood vessels in the tumors and slows down tumor growth and metastasis [73]. Atezolizumab on the other hand can reactivate $CD8^+$ T cells, by blocking the interaction of cancer cells with CD8 T cells through the PD-L1/PD-1 axis. These findings further classified the presented tumor models into the immune-active subclass [6], and demonstrated the practicality of the mouse models for the development of novel immune and anti-angiogenic therapies.

Ultimately, we conducted a comparative analysis between our model's responsiveness to AtezoBev and other studies/models using similar therapeutic strategy. For this analysis we selected available literature that tested AtezoBev (or similar therapies) in both, different HCC and non-HCC models. On average, combination anti-vascular and immune-checkpoint inhibitor therapy led to 71 % reduction in tumor size and 106 % increase of survival (Table S2) [74–79]. Importantly, our study displayed responsiveness within the ranges observed in literature, without being neither at the low- nor at the high-end of the responsiveness range. Interestingly, AtezoBev demonstrated comparable efficacies in Hepa1–6 models compared to Dt81Hepa1–6 models [74,75].

4. Discussion

Our study aimed to establish and characterize an HCC model based on intrasplenic injection of syngeneic HCC cells (Dt81Hepa1–6) for studying tumor development in both cirrhotic and non-cirrhotic livers of immunocompetent mice. After 4 weeks post tumor inoculation we found that both, HCC and (C-)HCC models, exhibited advanced stage diseases (Fig. 1E-G), with comparable degrees of desmoplasia (Fig. 3), vascularization (Fig. 4), immune cell infiltration (Fig. 5) and response to AtezoBev (Fig. 6). In patients, HCC typically develops due to long-term liver injuries that arise from hepatitis virus infection, alcohol abuse, or high-fat diet [80]. The prolonged liver damage takes up to 20 years to manifest as chronic disease and be diagnosed as cirrhosis, with another 10 years to develop into a malignancy and be then identified as HCC [81, 82]. In our model, we have captured both the cirrhotic and non-cirrhotic scenarios, by opting to induce liver damage or not, achieving this within a much shorter time frame (i.e., 4 weeks for HCC and 11 weeks for C-HCC model), at a 100 % tumor-development yield. In contrast to other models, which are time-intensive and result in heterogeneous tumor growth [83], our model exhibits homogeneous and robust tumor growth. This feature allows researchers to control the timing of their *in vivo* studies, leading to more reproducible results with a lower number of animals required for experiments, which is in line with the official animal welfare guidelines in Europe [84]. The tumor growth and tumor load are additionally well-controllable depending on the amount of injected cells, which is a clear advantage compared to genetically induced models with variable growth and variable phenotypes [85]. Furthermore, the intrasplenic injection has been proven to be advantageous over intrahepatic injection, as it limits the probability of procedural complications (e.g., infections or bleeding), and from a practical point of view, is relatively easy to learn and perform. This method results in the robust and homogenous growth of multiple lesions in the liver through seeding the tumor cells via the splenic vein, rather than the development of a single tumor mass, again resembling the clinical occurrence of HCC [22,23]. Another advantage is the use of the highly tumorigenic HCC cell line Dt81Hepa1–6, which overexpresses key genes observed in human HCC and can be used to study HCC cell behavior *in vitro* [23,32]. Last but not least, tumor growth takes place in immunocompetent mice, which is a requirement for immunological studies and screening of novel immunotherapies aimed towards the modulation of adaptive immunity, e.g., immune checkpoint inhibition [23,65,86]. Our tumors responded well to the current first-line combination therapy; a fact that strengthens its relevance for evaluating clinically relevant strategies.

At this point, it is important to acknowledge other models useful for preclinical research, e.g., patient-derived xenograft (PDX) models or humanized mouse models. In PDX tumor models, patient-derived material is usually engrafted into immunocompromised mice, allowing the study of cancer biology and test drug responses in a setting that mimics the human TME [87]. Humanized mouse models are developed by engrafting human hematopoietic stem cells or peripheral blood mononuclear cells into immunodeficient mice, enabling the simulation of a human-like immune response. Ultimately, both models can be combined, resulting in patient-derived material engrafted in humanized mice [88]. Nevertheless, these models come with their own limitations. PDX models rely on patient material, which is often limited and varies amongst patients and among lesions of the same patient. In addition, although such models can be used for personalized medicine strategies, their use in immunotherapy research is restricted, as the tumors grow in athymic immunodeficient nude mice lacking adaptive immunity. Humanized mouse models enable immunotherapy studies but face additional technical challenges. These include incomplete reconstitution of the human immune system due to murine cytokine incompatibility, limited immune cell development, and risks of graft-versus-host disease, due to human immune cells recognizing mouse tissue as foreign. Finally, all above-described methods to establish PDX, humanized mouse models and their combinations, are complex, time-consuming, expensive and require advanced technical expertise for their successful implementation, all of which can limit their widespread application [88].

HCC develops as a result of different causes of chronic liver damage, thus explaining the heterogeneous mutanome of HCC observed in patients [89–92]. Changes in dietary habits, e.g. western diet, contribute to a rising incidence of HCC in MASH patients without cirrhosis, however cirrhosis remains to be the strongest risk factor for HCC [6,93]. This diverse HCC occurrence seen in the clinic has been considered in our work, by introducing optional CCl_4 gavage, allowing subsequent tumor inoculation into a liver with or without chronic liver damage. The pro-fibrotic effect of CCl_4 has parallels to alcohol-induced cirrhosis, which is by far the most prevalent etiology for cirrhosis in the western world [94]. We observed an increased tumor load in mice with CCl_4-induced cirrhosis (Section 3.1). This is well in line with previous reports showing that the presence of organ fibrosis in both lungs and liver increases the ability and probability of circulating breast cancer cells to colonize and grow in metastatic models [95]. We showed that the cirrhotic liver displays a favorable microenvironment for the proliferation of cancer cells through excessive secretion of ECM and growth factors, the formation of capillary blood vessels, and dampening of the immune cells of the liver through the CTLA-4 and PD-L1 axes (Section 3.2). Additionally, AFP is thought to have a pro-oncogenic effect [96,97]. As the amount of cancer cell secretion increases, so does the release of AFP, creating a positive feedback loop in which more AFP stimulates further growth and proliferation of cancer cells.

Tumors in our model developed multifocally with desmoplasia, elevated vascularization, and immunological activation at relevant levels in agreement with other models reported in literature [62]. We have shown that angiogenesis plays an important role in HCC. This is additionally validated by indirect inhibition of angiogenesis through MFAP-5 silencing. MFAP-5 (microfibrillar-associated protein 5), a glycoprotein produced by CAF, is shown to promote proliferation in fibroblasts, HCC cells, and endothelial cells, thereby driving angiogenesis in the TME. Intravenous administration of anti-MFAP-5 silencing RNA showed a strong antitumor effect by inhibiting angiogenesis through MFAP-5 RNA interference, highlighting the role of angiogenesis in tumor growth [42]. The extensive TME analysis, presented in this work, reflects the possibilities for (combination) therapy development to target components of the ECM, vasculature and immune cells in the TME in various stages of tumor development.

Additionally, our model demonstrated responsiveness to combined anti-VEGF/anti-PD-L1 therapy. Our comparative analysis showed that response rates were close to the ones reported in other studies, especially showing similarities to response rates of Hepa1–6 models (Table S2). As a result of the strong antitumor effect with AtezoBev, the standard first-line therapy targeting unresectable HCC, our models can help to develop even more effective therapeutic approaches for the clinics.

In conclusion, we present a robust and easy-to-handle intrasplenic injection model for multifocal HCC based on hepatotropic tumor cells with histologic and genetic alterations found in human HCC. Due to the combination of the CCl_4-induced parenchymal damage and multifocal tumor growth pattern, our model closely reflects the tumor microenvironment of HCC in patients. Combining CCl_4 with HCC cell inoculation, accelerated tumor growth, resembling the development of HCC in cirrhotic livers. The model showed a strong therapeutic response to immuno- and anti-angiogenic therapy. Thus, our model could be valuable for rapid screening of modern anticancer and immune therapies.

Ethical approval

Animal studies were approved by local authorities (Landesuntersuchungsamt (LUA) Rhineland-Palatinate, Germany) with the reference number G20–1–130.

CRediT authorship contribution statement

Stephan Grabbe: Writing – review & editing. **Paul Schneider:** Writing – review & editing, Validation, Methodology, Investigation, Formal analysis. **Mustafa Diken:** Writing – review & editing. **Fabian Kiessling:** Writing – review & editing, Validation. **Özlem Akilli:** Investigation. **Barbara Schörs:** Writing – review & editing, Data curation. **Feyza Durak:** Writing – review & editing, Investigation. **Leonard Kaps:** Writing – review & editing, Supervision, Conceptualization. **Federica De Lorenzi:** Writing – review & editing, Validation. **Alexandros Marios Sofias:** Writing – review & editing, Supervision, Conceptualization. **Jenny Schunke:** Writing – review & editing, Investigation. **Twan Lammers:** Writing – review & editing, Supervision, Conceptualization. **Michael Fichter:** Writing – review & editing, Investigation. **Jörn M. Schattenberg:** Writing – review & editing. **Panayiotis Kordeves:** Writing – review & editing, Investigation. **Karina Benderski:** Writing – original draft, Visualization, Validation, Methodology, Investigation, Formal analysis. **Matthias Bros:** Writing – review & editing, Methodology.

Declaration of Competing Interest

The authors declare the following financial interests/personal relationships which may be considered as potential competing interests: LK declares receiving travel expenses and speaker honoraria from Gilead science (Foster city, USA) and Takeda (Doshomachi, Japan). JMS declares consultant honorary from Alentis, Alexion, Altimmune, Astra Zeneca, 89Bio, Bionorica, Boehringer Ingelheim, Gilead Sciences, GSK, Ipsen, Inventiva Pharma, Madrigal Pharmaceuticals, Lilly, MSD, Northsea Therapeutics, Novartis, Novo Nordisk, Pfizer, Roche, Sanofi, and Siemens Healthineers. JMS declares speaker honorarium from AbbVie, Academic Medical Education (AME), Boehringer Ingelheim, Echosens, Forum für Medizinische Fortbildung (FOMF), Gilead Sciences, MedicalTribune, MedPublico GmbH, MedScape, Novo Nordisk, Madrigal Pharmaceuticals, Stockholder options: AGED diagnostics, and Hepta Bio. The other authors have no conflicts of interest to declare.

Acknowledgements

The authors gratefully acknowledge financial support by the German Research Foundation (DFG; SFB1066, SFB1382, Excellence initiative - JPI RWTH 2021), and the European Research Council (ERC; Consolidator Grant Meta-Targeting). Active support was also given by the Two-Photon Imaging Core Facility and Immunochemistry at the IZKF at the Faculty of Medicine at RWTH Aachen University. We would like to offer special thanks to the group of M. Bilodeau (Montreal, Canada) and Dominik Siegl who provided us with the HCC cell line Dt81Hepa1-6.

Author contribution

LK, AMS, and TL conceptualized, structured, and supervised the work. KB, PS, PK, FD and ÖA performed the experiments. MF, JS, and MB assisted in the performance of *in vivo* experiments. KB, PS, PK, and BS analyzed the data. LK, AMS, TL, KB, PS, FDL, FK, MD, SG and JMS interpreted the data. KB drafted the first version of the manuscript. PS critically revised, corrected, and commented on the manuscript. All authors read, reviewed, and approved the final version of the manuscript.

Appendix A. Supporting information

Supplementary data associated with this article can be found in the online version at doi:10.1016/j.phrs.2024.107560.

References

[1] K.A. McGlynn, J.L. Petrick, H.B. El-Serag, Epidemiology of hepatocellular carcinoma, Hepatology 73 (2021) 4–13.

[2] H. Rumgay, et al., Global burden of primary liver cancer in 2020 and predictions to 2040, J. Hepatol. 77 (2022) 1598–1606.

[3] M.R. Toh, et al., Global epidemiology and genetics of hepatocellular carcinoma, Gastroenterology 164 (2023) 766–782.

[4] Y.M. Tsui, L.K. Chan, I.O.L. Ng, Cancer stemness in hepatocellular carcinoma: mechanisms and translational potential, Br. J. Cancer 122 (2020) 1428–1440.

[5] F. Feng, et al., Lactylome analysis unveils lactylation-dependent mechanisms of stemness remodeling in the liver cancer stem cells, Adv. Sci. 2405975 (2024) 1–15.

[6] J.M. Llovet, et al., Hepatocellular carcinoma, Nat. Rev. Dis. Prim. 7 (2021).

[7] A.M. Sofias, et al., Therapeutic and diagnostic targeting of fibrosis in metabolic, proliferative and viral disorders, Adv. Drug Deliv. Rev. 175 (2021) 113831.

[8] X. Xie, et al., Correlation analysis of metabolic characteristics and the risk of metabolic-associated fatty liver disease - related hepatocellular carcinoma, Sci. Rep. 12 (2022) 1–8.

[9] L. Zampaglione, J. Ferrari, N. Vietti Violi, N. Goossens, The Role of Extrahepatic Features on the Development and Management of Hepatocellular Carcinoma in Steatotic Liver Disease, Discov. Med. 36 (2024) 1127.

[10] H. Zhang, W. Zhang, L. Jiang, Y. Chen, Recent advances in systemic therapy for hepatocellular carcinoma, Biomark. Res. 2021 101 10 (2022) 1–21.

[11] E. Kim, P. Viatour, Hepatocellular carcinoma: old friends and new tricks, Exp. Mol. Med. 52 (2020) 1898–1907.

[12] J.M. Llovet, et al., Immunotherapies for hepatocellular carcinoma, Nat. Rev. Clin. Oncol. 19 (2022) 151–172.

[13] L. Kaps, D. Schuppan, Targeting cancer associated fibroblasts in liver fibrosis and liver cancer using nanocarriers, Cells 9 (2020) 1–23.

[14] Z. Sas, E. Cendrowicz, I. Weinhäuser, T.P. Rygiel, Tumor microenvironment of hepatocellular carcinoma: challenges and opportunities for new treatment options, Int. J. Mol. Sci. 23 (2022).

[15] C. Lu, et al., Current perspectives on the immunosuppressive tumor microenvironment in hepatocellular carcinoma: challenges and opportunities, Mol. Cancer 18 (2019) 1–12.

[16] Z.J. Brown, B. Heinrich, T.F. Greten, Mouse models of hepatocellular carcinoma: an overview and highlights for immunotherapy research, Nat. Rev. Gastroenterol. Hepatol. 15 (2018) 536–554.

[17] T. Fujii, et al., Mouse model of carbon tetrachloride induced liver fibrosis: histopathological changes and expression of CD133 and epidermal growth factor, BMC Gastroenterol. 10 (2010).

[18] T. Uehara, I.P. Pogribny, I. Rusyn, The DEN and CCl4-induced mouse model of fibrosis and inflammation-associated hepatocellular carcinoma, 14.30.1-14.30.10, Curr. Protoc. Pharmacol. (2014), 14.30.1-14.30.10.

[19] N. Gehrke, et al., Hepatic B cell leukemia-3 suppresses chemically-induced hepatocarcinogenesis in mice through altered MAPK and NF-κB activation, Oncotarget 8 (2017) 56095–56109.

[20] C.Y. Gu, T.K.W. Lee, Preclinical mouse models of hepatocellular carcinoma: an overview and update, Exp. Cell Res. 412 (2022) 113042.

[21] H. Kasashima, et al., An orthotopic implantation mouse model of hepatocellular carcinoma with underlying liver steatosis, STAR Protoc. 1 (2020) 100185.

[22] L.E. McVeigh, et al., Development of orthotopic tumour models using ultrasound-guided intrahepatic injection, Sci. Rep. 9 (2019) 1–9.

[23] B. Lacoste, V.A. Raymond, S. Cassim, P. Lapierre, M. Bilodeau, Highly tumorigenic hepatocellular carcinoma cell line with cancer stem cell-like properties, PLoS One 12 (2017) e0171215.

[24] S.W. Wingett, S. Andrews, Fastq screen: a tool for multi-genome mapping and quality control, F1000Research 7 (2018) 1–14.

[25] N.L. Bray, H. Pimentel, P. Melsted, L. Pachter, Near-optimal probabilistic RNA-seq quantification, Nat. Biotechnol. 34 (2016) 525–527.

[26] M.I. Love, W. Huber, S. Anders, Moderated estimation of fold change and dispersion for RNA-seq data with DESeq2, Genome Biol. 15 (2014) 1–21.

[27] A. Zhu, J.G. Ibrahim, M.I. Love, Heavy-Tailed prior distributions for sequence count data: removing the noise and preserving large differences, Bioinformatics 35 (2019) 2084–2092.

[28] Y. Benjamini, Y. Hochberg, Controlling the false discovery rate - a practical and powerful approach to multiple testing, J. R. Stat. Soc. Ser. B 57 (1995) 289–300.

[29] L. Kaps, et al., In vivo gene-silencing in fibrotic liver by siRNA-loaded cationic nanohydrogel particles, Adv. Healthc. Mater. 4 (2015) 2809–2815.

[30] R.D. Cardiff, C.H. Miller, R.J. Munn, Manual hematoxylin and eosin staining of mouse tissue sections, Cold Spring Harb. Protoc. 2014 (2014) 655–658.

[31] H. Liu, J. Shen, K. Lu, IL-6 and PD-L1 blockade combination inhibits hepatocellular carcinoma cancer development in mouse model, Biochem. Biophys. Res. Commun. 486 (2017) 239–244.

[32] S. Hua, et al., Identification of hub genes in hepatocellular carcinoma using integrated bioinformatic analysis, Aging Albany NY 12 (2020) 5439–5468.

[33] X. Hu, R. Chen, Q. Wei, X. Xu, The landscape of alpha fetoprotein in hepatocellular carcinoma: where are we? Int. J. Biol. Sci. 18 (2022) 536–551.

[34] H. Bösmüller, et al., Microvessel density and angiogenesis in primary hepatic malignancies: differential expression of CD31 and VEGFR-2 in hepatocellular carcinoma and intrahepatic cholangiocarcinoma, Pathol. Res. Pract. 214 (2018) 1136–1141.

[35] L. Wullkopf, et al., Cancer cells' ability to mechanically adjust to extracellular matrix stiffness correlates with their invasive potential, Mol. Biol. Cell 29 (2018) 2378–2385.

[36] G. Zhao, et al., Mechanical stiffness of liver tissues in relation to integrin β1 expression may influence the development of hepatic cirrhosis and hepatocellular carcinoma, J. Surg. Oncol. 102 (2010) 482–489.

[37] G. Giannelli, E. Villa, M. Lahn, Transforming growth factor-β as a therapeutic target in hepatocellular carcinoma, Cancer Res. 74 (2014) 1890–1894.

[38] H.P. Fischer, U. Flucke, H. Zhou, Pathology along the liver sinusoids: endothelial and perisinusoidal findings, Pathologe 29 (2008) 37–46.

[39] Y. Xing, T. Zhao, X. Gao, Y. Wu, Liver X receptor α is essential for the capillarization of liver sinusoidal endothelial cells in liver injury, Sci. Rep. 6 (2016) 1–11.

[40] B. Foglia, et al., Hypoxia, hypoxia-inducible factors and liver fibrosis, Cells 10 (2021).

[41] Z. Chen, F. Han, Y. Du, H. Shi, W. Zhou, Hypoxic microenvironment in cancer: molecular mechanisms and therapeutic interventions, Signal Transduct. Target. Ther. 8 (2023).

[42] P. Schneider, et al., Multicompartment polyion complex micelles based on triblock polypept(o)ides mediate efficient siRNA delivery to cancer-associated fibroblasts for antistromal therapy of hepatocellular carcinoma, Adv. Mater. 2404784 (2024) 1–18.

[43] E. Witsch, M. Sela, Y. Yarden, Roles for growth factors in cancer progression, Physiology 25 (2010) 85–101.

[44] T. Kanda, R. Sasaki-Tanaka, S. Terai, Inflammation of the liver, HCC development and HCC establishment, Hepatol. Int. 18 (2024) 1090–1092.

[45] E. Hintermann, U. Christen, The many roles of cell Adhesion molecules in hepatic fibrosis, Cells 8 (2019).

[46] T. Lange, et al., Tumor cell E-selectin ligands determine partialefficacy of bortezomib on spontaneous lung metastasis formation of solid human tumors in vivo, Mol. Ther. 30 (2022) 1536–1552.

[47] C. Bosteels, et al., Inflammatory Type 2 cDCs acquire features of cDC1s and macrophages to orchestrate immunity to respiratory virus infection, Immunity 52 (2020) 1039–1056.e9.

[48] Y. Wen, J. Lambrecht, C. Ju, F. Tacke, Hepatic macrophages in liver homeostasis and diseases-diversity, plasticity and therapeutic opportunities, Cell. Mol. Immunol. 18 (2021) 45–56.

[49] M. Oshi, et al., M1 Macrophage and M1/M2 ratio defined by transcriptomic signatures resemble only part of their conventional clinical characteristics in breast cancer, Sci. Rep. 10 (2020) 1–12.

[50] R. Liu, et al., Harnessing metabolism of hepatic macrophages to aid liver regeneration, Cell Death Dis. 14 (2023) 1–10.

[51] M.L. Alegre, K.A. Frauwirth, C.B. Thompson, T-cell regulation by CD28 and CTLA-4, Nat. Rev. Immunol. 1 (2001) 220–228.

[52] K.-J. Wu, et al., Regulatory T cells (Tregs) in liver fibrosis, Cell Death Discov. 9 (2023) 1–8.

[53] D.D. Cissell, J.M. Link, J.C. Hu, K.A. Athanasiou, A modified hydroxyproline assay based on hydrochloric acid in ehrlich's solution accurately measures tissue collagen content, Tissue Eng. Part C Methods 23 (2017) 243–250.

[54] Y. Yuan, Y.C. Jiang, C.K. Sun, Q.M. Chen, Role of the tumor microenvironment in tumor progression and the clinical applications, Oncol. Rep. 35 (2016) 2499–2515.

[55] A.M. Roy, R. Iyer, S. Chakraborty, The extracellular matrix in hepatocellular carcinoma: mechanisms and therapeutic vulnerability, Cell Rep. Med. 4 (2023) 101170.

[56] B. Wolf, et al., Desmoplasia in cervical cancer is associated with a more aggressive tumor phenotype, Sci. Rep. 13 (2023) 1–9.

[57] D. Katenkamp, T.M.H. Kosmehl, H. Kosmehl, CD34-Nachweis ± ein immunhistochemischer Beitrag zur Differentialdiagnose von Weichgewebstumoren, Pathologe 17 (1996) 195–201.

[58] C. Géraud, et al., Liver sinusoidal endothelium: a microenvironment-dependent differentiation program in rat including the novel junctional protein liver endothelial differentiation-associated protein-1, Hepatology 52 (2010) 313–326.

[59] Q. Zhang, J. Wu, X. Bai, T. Liang, Evaluation of INtra-tumoral Vascularization in Hepatocellular Carcinomas, Front. Med. 7 (2020) 1–9.

[60] C. Han, T. Liu, R. Yin, Biomarkers for cancer-associated fibroblasts, Biomark. Res. 2021 101 (2020) 1–8.

[61] M.S. Hussain, et al., Non-coding RNA mediated regulation of PI3K/Akt pathway in hepatocellular carcinoma: therapeutic perspectives, Pathol. Res. Pract. 258 (2024) 155303.

[62] F. Heindryckx, et al., Kinetics of angiogenic changes in a new mouse model for hepatocellular carcinoma, Mol. Cancer 9 (2010) 1–14.

[63] L.Q. Kong, et al., The clinical significance of the CD163+ and CD68+ macrophages in patients with hepatocellular carcinoma, PLoS One 8 (2013).

[64] C.C. Hedrick, I. Malanchi, Neutrophils in cancer: heterogeneous and multifaceted, Nat. Rev. Immunol. 22 (2022) 173–187.

[65] D. Geh, et al., Neutrophils as potential therapeutic targets in hepatocellular carcinoma, Nat. Rev. Gastroenterol. Hepatol. 19 (2022) 257–273.

[66] N.L. Tran, G. Sitia, New players in non-alcoholic fatty liver disease induced carcinogenesis: lipid dysregulation impairs liver immune surveillance, HepatoBiliary Surg. Nutr. 5 (2016) 511–514.

[67] G. Parmiani, A. Anichini, T cell infiltration and prognosis in HCC patients, J. Hepatol. 45 (2006) 178–181.

[68] N. El Menshawy, et al., CD4/CD8 Ratio could be predictor of burden hepatocellular carcinoma in Egyptian chronic hepatitis C after combined sofosbuvir and daclatasvir therapy, Afr. Health Sci. 23 (2023) 198–212.

[69] A.J. Boutilier, S.F. Elsawa, Macrophage polarization states in the tumor microenvironment, Int. J. Mol. Sci. 22 (2021).

[70] W.G. Lesniak, et al., PD-L1 detection in tumors using [64Cu]Atezolizumab with PET, Bioconjug. Chem. 27 (2016) 2103–2110.

[71] Z.X. Zhao, et al., Inhibition of growth and metastasis of tumor in nude mice after intraperitoneal injection of bevacizumab, Orthop. Surg. 8 (2016) 234–240.

[72] K. Hollanders, et al., Bevacizumab revisited: Its use in different mouse models of ocular pathologies, Curr. Eye Res. 40 (2015) 611–621.

[73] V. Loizzi, et al., Biological pathways involved in tumor angiogenesis and bevacizumab based anti-angiogenic therapy with special references to ovarian cancer, Int. J. Mol. Sci. 18 (2017) 1–11.

[74] H. Deng, et al., Dual vascular endothelial growth factor receptor and fibroblast growth factor receptor inhibition elicits antitumor immunity and enhances programmed cell death-1 checkpoint blockade in hepatocellular carcinoma, Liver Cancer 9 (2020) 338–357.

[75] S. Li, et al., Low-dose radiotherapy combined with dual PD-L1 and VEGFA blockade elicits antitumor response in hepatocellular carcinoma mediated by activated intratumoral CD8+ exhausted-like T cells, Nat. Commun. 14 (2023).

[76] K. Shigeta, et al., Dual programmed death receptor-1 and vascular endothelial growth factor receptor-2 blockade promotes vascular normalization and enhances antitumor immune responses in hepatocellular carcinoma, Hepatology 71 (2020) 1247–1261.

[77] L. Meder, et al., Combined VEGF and PD-L1 blockade displays synergistic treatment effects in an autochthonous mouse model of small cell lung cancer, Cancer Res 78 (2018) 4270–4281.

[78] N. Ishikura, M. Sugimoto, K. Yorozu, M. Kurasawa, O. Kondoh, Anti-VEGF antibody triggers the effect of anti-PD-L1 antibody in PD-L1low and immune desert-like mouse tumors, Oncol. Rep. 47 (2022) 1–10.

[79] A.L. Cheng, et al., Updated efficacy and safety data from IMbrave150: atezolizumab plus bevacizumab vs. sorafenib for unresectable hepatocellular carcinoma, J. Hepatol. 76 (2022) 862–873.

[80] S. Dam-Larsen, et al., Long term prognosis of fatty liver: risk of chronic liver disease and death, Gut 53 (2004) 750–755.

[81] A. Armandi, E. Bugianesi, Natural history of NASH, Liver Int. 41 (2021) 78–82.

[82] P.J. Johnson, A. Kalyuzhnyy, E. Boswell, H. Toyoda, Progression of chronic liver disease to hepatocellular carcinoma: implications for surveillance and management, BJC Rep. 2 (2024) 1–7.

[83] A. Blidisel, et al., Experimental models of hepatocellular carcinoma—a preclinical perspective, Cancers 13 (2021).

[84] R. Stilliing, L. Berg, J. Wilken, Initiat. Transpar. Tierversuche: Netzw. F. üR. Eine Inf. Debatte (2024). 〈https://www.tierversuche-verstehen.de/〉.

[85] Z.M. Jilkova, K. Kurma, T. Decaens, Animal models of hepatocellular carcinoma: the role of immune system and tumor microenvironment, Cancers 11 (2019).

[86] D.J. Zabransky, et al., Profil. syngeneic mouse HCC Tumor Models a Framew. Under anti–PD-1 sensitive Tumor Microenviron. 77 (2023) 1566–1579.

[87] Y. Liu, et al., Patient-derived xenograft models in cancer therapy: technologies and applications, Signal Transduct. Target. Ther. 8 (2023).

[88] R. Kumari, G. Feuer, L. Bourré, Humanized mouse models for immuno-oncology drug discovery, Curr. Protoc. 3 (2023) 1–23.

[89] Thorgeirsson, S.S. & Grisham, J.W. Molecular pathogenesis of human hepatocellular carcinoma. **31**, (2002).

[90] Vyas, M. & Jain, D. An update on subtypes of hepatocellular carcinoma: From morphology to molecular. (2021).

[91] Craig, A.J., Felden, J.Von, Sarcognato, S. & Villanueva, A. Tumour evolution in hepatocellular carcinoma. Nat. Rev. Gastroenterol. Hepatol.

[92] M.S. Torbenson, Hepatocellular carcinoma: making sense of morphological heterogeneity, growth patterns,and subtypes, Hum. Pathol. 112 (2021) 86–101.

[93] H. Xu, et al., SUMO1 modification of methyltransferase-like 3 promotes tumor progression via regulating Snail mRNA homeostasis in hepatocellular carcinoma, Theranostics 10 (2020) 5671–5686.

[94] F. Stickel, C. Datz, J. Hampe, R. Bataller, Pathophysiology and management of alcoholic liver disease: Update 2016, Gut Liver 11 (2017) 173–188.

[95] Y.F.I. Setargew, K. Wyllie, R.D. Grant, J.L. Chitty, T.R. Cox, Targeting lysyl oxidase family meditated matrix cross-linking as an anti-stromal therapy in solid tumours, Cancers (2021).

[96] Y. Lu, et al., Alpha fetoprotein plays a critical role in promoting metastasis of hepatocellular carcinoma cells, J. Cell. Mol. Med. 20 (2016) 549–558.

[97] P.R. Galle, et al., Biology and significance of alpha-fetoprotein in hepatocellular carcinoma, Liver Int. 39 (2019) 2214–2229.